

NISTIR 6747

Validation and Modification of the 4SIGHT Computer Program

Kenneth A. Snyder



United States Department of Commerce
Technology Administration
National Institute of Standards and Technology

NISTIR 6747

Validation and Modification of the 4SIGHT Computer Program

Kenneth A. Snyder
Building Materials Division
Building and Fire Research Laboratory
National Institute of Standards and Technology
Gaithersburg, MD 20899-8621

Sponsor:
U.S. Nuclear Regulatory Commission

May 2001



U.S. Department of Commerce
Donald L. Evans, *Secretary*
National Institute of Standards and Technology
Karen H. Brown, *Acting Director*

Abstract

The original version of the 4SIGHT computer program was written to facilitate the performance assessment of buried concrete structures based deterministic calculations of service life, using data supplied by the user. In an effort to ensure reliability in the results, a means of validation was required. Since the results from the calculations depend strongly on the diffusive and advective transport of ionic species, validating the transport portion of 4SIGHT was paramount.

The validation of the transport portion of 4SIGHT used both reference and laboratory data. The reference data include electrolyte densities, activity coefficients, and binary salt diffusion coefficients. The laboratory experiments included diffusion experiments performed on relatively inert ceramic frits, using a range of ionic species and concentrations. The laboratory experiments were also used to confirm the fundamental assumption that multi-species transport in non-reacting systems can be characterized by two numbers, the porosity and the formation factor, regardless of the number of diffusing species.

A default analysis for estimating the spacing and thickness of flexural and drying shrinkage cracks was added to 4SIGHT. The flexural cracks are calculated from a rudimentary structural analysis that assumes the roof of the vault acts as a one-way slab. The drying shrinkage cracks are estimated, in large part, from the total water content of the concrete mixture, the exposure environment, and the geometry of the slab. The subsequent predicted crack widths, crack spacings, and location of the neutral axis, are used to predict the bulk permeability of the concrete structure as a function of depth; the portion above the neutral axis being uncracked, the portion below the neutral axis being cracked.

Another addition to 4SIGHT was the means to perform a Monte Carlo calculation, based on parameter uncertainty, of the duration of useful service. The service life calculation is repeated multiple times using a random number generator to calculate random deviates for the physical parameters. The results can then be used to make a probabilistic statement about the performance of the concrete structure.

The resulting computer program is state-of-the-art attempt to characterize both the response of a concrete to its environment. However, there can be no assurances that the model is exact for every scenario possible, regardless of parameter uncertainty. Therefore, in cases that concern public safety, the only way to confirm the response of the concrete to its environment is through continuous monitoring and periodic testing. The computer program, in these circumstances, can also serve as a useful tool in establishing a testing monitoring protocol. The spatial and temporal distribution of the monitoring and testing protocol can be established using the computer program as a guide.

Keywords: building technology; concrete; degradation; Monte Carlo; parameter uncertainty; service life; transport

Contents

Abstract	iii
1 Introduction	1
2 Degradation Validation Examples	3
2.1 Literature	3
2.1.1 Leaching	4
2.1.2 Chloride Diffusion	6
2.1.3 HETEK Model	8
3 Transport	10
3.1 Transport Equation	10
3.1.1 Electrical Measurements	11
3.1.2 Diffusive Ionic Flux	13
3.1.3 Formation Factor	13
3.1.4 Conservation Equation	15
3.1.5 Complete Transport Equation	18
4 Transport Validation	19
4.1 Reference Data	19
4.1.1 Electrolyte Density	19
4.1.2 Activity Coefficient	20
4.1.3 Electrolyte Diffusion Coefficient	21
4.2 Laboratory Data	22
4.2.1 Ceramic Frit	23
4.2.2 Experimental Setup	24
4.2.3 Analysis	24
4.2.4 Formation Factor Measurement	25
4.3 Formation Factor vs. Diffusion Coefficient	26
4.3.1 Multi-Species	29
4.4 Summary	34
5 Parameter Uncertainty	36
5.1 Random Deviates	36
5.2 Distributions	36
5.2.1 Delta Function	36
5.2.2 Uniform Distribution	37
5.2.3 Gaussian Distribution	37
5.2.4 Lognormal Distribution	37
5.3 Output: Cumulative Distribution	38

6	Significance of Cracks	40
6.1	Internal Body Force	40
6.2	Sorptivity	41
6.3	Break-Through Pressure	42
6.4	Transport Through Cracks	43
6.4.1	Residence Time	43
6.4.2	Evaporative Mass Transfer	44
7	Predicting Drying Shrinkage and Flexural Cracks	46
7.1	Cracked Reinforced Concrete	47
7.1.1	Crack Model	47
7.1.2	Composite Permeability	48
7.1.3	Composite Permeability Model	49
7.2	Flexural Crack Model	50
7.3	Shrinkage Crack Model	50
7.4	Design Example	51
7.4.1	Mixture Design	52
7.4.2	Concrete Properties	52
7.4.3	Steel Properties	55
7.4.4	Reinforcement Ratio Requirements	55
7.4.5	Roof Geometry	56
7.4.6	Positive Moment	57
7.4.7	Uncracked Analysis	57
7.4.8	Cracked Section Analysis	59
7.4.9	Simplified Composite Permeability	62
7.5	Probabilistic Approach	62
7.5.1	Initial Material Parameters	63
7.5.2	Results	64
8	User's Guide	68
8.1	Input File	68
9	Summary	73

List of Tables

1	Estimated and reported diffusion coefficients, and estimated paste porosities, for the three concrete mixtures considered.	8
2	The measured diffusion coefficients (D_{HETEK}) and the estimated diffusion coefficient (D_{4SIGHT}) for different values of water-cement ratio (w/c).	9
3	Comparison of diffusion coefficients D from the computer program (CP) and handbook (HB) (Ref. [30]) values for various salts in aqueous solution.	22
4	The values for the slope (AD_b/L) of the experimental data shown in Fig. 11. Also shown is the ratio D^s/D_b , using D^s for iodide. The uncertainties shown for the slopes are the estimated standard deviation reported by the statistical software, and also characterize the uncertainty in the ratio D^s/D_b reported.	28
5	Measured and calculated formation factors from impedance spectroscopy (F_{IS}), computer simulation (F_{sim}), and apparent diffusivity (D^s/D_b) using D^s for iodide.	29
6	Absolute value of the slopes calculated from the data for the KCl/KI and the NaCl/KI systems in Figs. 12, regressed to a linear model. The uncertainties shown are the estimated from standard deviations reported by the regression software, with a corresponding coverage factor of $k = 1$	31
7	Magnitude of the slope for data shown in Fig. 13(a), regressed to Eqn. 35 for $t(v_1^{-1} + v_2^{-1}) < 8 \text{ h/cm}^3$. For each system, the KI concentration was 0.10 mol/L. Also shown are the values for the formation factor F used to produce the solid curves Fig. 13(b). The uncertainties shown are the estimated from standard deviations reported by the regression software, with a corresponding coverage factor of $k = 1$	31
8	Material parameters a concrete with w/c = 0.45, estimated from equations in Ref. [1]. (Default degree of hydration $\alpha = 0.85$)	40
9	Parameters for the composite permeability calculation for m cracks of width w . The crack model refers to that shown in either Fig. 19(a) or Fig. 19(b).	50
10	The mean and associated coefficient of variation (CoV) for the input parameters that would be used in an uncertainty analysis of flexural and shrinkage cracking.	64

List of Figures

1	Sample porosity, based upon pores 1 μm to 10 μm in size, as a function of distance from the exposure surface. Graph taken from Trägøardh and Lagerblad [5]	4
2	Chloride concentration (percent by mass fraction of cement) for the three concrete mixtures (solid symbols). The concretes are made with ordinary sulfate resistant cements. The curves are estimates by 4SIGHT. Data are reproduced from Sandberg et al. [6].	7
3	Schematic of the bulk flux and the pore flux, characterized by the bulk velocity \mathbf{v}_b and pore velocity \mathbf{v}_p , due to a pressure hydrostatic pressure drop of $P_1 - P_2$ across the specimen.	15
4	Schematic for ionic flux conservation through a volume of unit area and differential width dx	17
5	Density of 1-1 electrolytes (a) and 1-2, 2-1, and 2-2 electrolytes (b) as a function of molarity. Data from the chemistry handbook appear as symbols. The predictions by 4SIGHT appear as solid curves.	19
6	Density of strong acids and bases. Data from the chemistry handbook appear as symbols. The predictions by 4SIGHT appear as solid curves. . .	20
7	Activity coefficient of chloride ions γ_{Cl^-} as a function of molality m for various electrolytes. The estimates by 4SIGHT are shown as solid curves. Results from the PHRQPITZ computer program [31] are shown as filled symbols. Data from the <i>CRC Handbook of Chemistry and Physics</i> [30] are shown as open symbols.	21
8	The pore solution conductivity σ_p and the corresponding bulk conductivity σ_b for the resin system of McDuff and Ellis [36] and the frit system used here.	23
9	Schematic of the constant gradient hypothesis across a sample with thickness L . Vessels 1 and 2 contain an aqueous electrolyte with target species concentrations c_1 and c_2 , and have volumes v_1 and v_2 , respectively. . . .	25
10	The conductivity cell apparatus(a) and the diffusion divided cell apparatus (b). The schematics depict the configuration of the two cylindrical glass vessels on either side of a mounted specimen. The system is sealed using rubber o-rings; the clamps are not shown. The apparatus differ only in the vertical platinum electrodes in the conductivity cell. The diameter of the specimen, the glass vessels, and the platinum electrodes are approximately 50 mm.	26
11	Concentration difference across each specimen as a function of time normalized by the vessel volumes. The experimental values are shown as filled symbols, the estimates by 4SIGHT are shown as solid curves. The measurement uncertainties would appear as the same size as the symbols, so are omitted for visual clarity. The value of Δ for the 1.0 mol/L KCl system is divided by ten in order to appear on the same scale as the other data.	27

12	Concentration difference Δ of iodide (filled symbols) for the KCl/KI and the NaCl/KI systems; the time t is scaled by the vessel volumes v_1 and v_2 . The quantity Δ_0 is the initial KI concentration. The lines shown are the result of the linear regression analyses reported in Table 6. The measurement uncertainties are approximately the size of the symbols used.	30
13	Measured concentration difference Δ of iodide (filled symbols) for constant 0.10 mol/L KI concentration and varying counter-diffusing species; the time t is scaled by the vessel volumes v_1 and v_2 . In (a) results from linear regression (solid lines) for $t(v_1^{-1} + v_2^{-1}) < 8$ h/cm ³ ; the calculated slopes are reported in Table 7. In (b) the electro-diffusion equation is used to estimate the formation factor F , the values of which are shown in Table 7. The error bars represent an estimated standard deviation.	32
14	The ratio of the apparent diffusion coefficient D^a to the microstructural diffusion coefficient D^μ (as calculated by 4SIGHT using Eqn. 14) of iodide for the various counter diffusing electrolytes, as a function of time t .	33
15	Experimental concentration difference Δ of each diffusing species in the (a) CaCl ₂ /KI, and the (b) K ₂ CO ₃ /KI systems, each as a function of time t . The experimental values are shown as filled symbols, and the curves are the values calculated by 4SIGHT. The error bars represent an estimated standard deviation.	34
16	The cumulative distribution function $G(t)$.	39
17	Schematic of water sorption in concrete. The hashed region represents a cross section, with pore radius R and liquid-air surface tension γ , with its bottom surface under water. To the right is a plot of the hydraulic pressure P as one traverses vertically through the pore. Negative pressure indicates water in tension.	41
18	Schematic of the hydraulic pressures in a porous material with a thin layer of water on its top surface and unsaturated air exposure on its bottom surface.	42
19	Composite models for the bulk permeability of the roof incorporating the uncracked permeability k_c , crack permeability k' , and having a number m cracks over the slab length L : (a) slabs with m cracks, each with width w ; (b) slabs with m_1 and m_2 cracks of width w_1 and w_2 , respectively.	48
20	Quantities for estimating shrinkage strain: (a) ultimate drying shrinkage strain under standard conditions; (b) factor γ_{cp} for duration of moist curing; (c) factor γ_ϕ for ambient relative humidity; and (d) factor $\gamma_{\nu s}$ for the volume to surface ratio.	53
21	Roof geometry used for analysis: (a) cross section showing location of steel reinforcement (filled circles); (b) transformed section used for uncracked analysis; (c) transformed section used for cracked analysis.	56
22	Depth of neutral axis c as a function of the reinforcement ratio ρ for the uncracked analysis.	59
23	Compressive stress f_c and tensile stress f_t as a function of the reinforcement ratio ρ , based on the uncracked analysis.	60

24	Cracked transformed section analysis: (a) relative depth of neutral axis λ ; (b) relative tensile stress f_t/f_y and compressive stress f_c/f'_c for the cracked section analysis, assuming linear elastic behavior.	61
25	Results of the cracking model: (a) The ratio of the shrinkage crack spacing L_s and the flexural crack spacing L_f ; (b) Flexural crack width w_f and shrinkage crack width w_s	62
26	Ratio of the composite permeability k^* to the uncracked concrete permeability k_c : (a) as a function of reinforcement ratio ρ , and (b) as a function of the relative depth to the neutral axis α	63
27	Probabilistic analysis results: (a) Relative depth of neutral axis λ ; (b) Relative tensile stress f_t/f_y and compressive stress f_c/f'_c for the cracked section analysis.	65
28	Results of the probabilistic analysis of the cracking models: (a) the ratio of the shrinkage crack spacing L_s to the flexural crack spacing L_f ; (b) flexural crack width w_f and shrinkage crack width w_s	66
29	From the probabilistic analysis, the ratio of the composite permeability k^* to the uncracked concrete permeability k_c	67

1 Introduction

The 4SIGHT computer program, first published in 1995 [1], was developed as a resource for estimating the service life of new underground concrete structures. The program was the first to use combined numerical models for ion transport, chemical reaction, and subsequent changes to transport coefficients to model the response of a concrete structure to its environment. Although the individual components of 4SIGHT duplicated previous work, the unique ensemble allowed 4SIGHT to model the synergistic degradation effects that may occur. While this approach is physically sound, the model remained to be validated in order to ensure confidence in the results.

The initial validation concept was to use samples from field concrete and compare the prediction of 4SIGHT to the actual response of the concrete. While conceptually sound, there were unforeseen pitfalls to such an approach. Since 4SIGHT was to be used to predict the performance over decades, and possibly centuries, comparable concrete data were needed. While such concretes exist, the documentation of these structure is either scarce or non-existent. Further, the environmental conditions that the concretes were subjected to were also difficult to quantify. These undetermined parameters were either estimated using other data within the report or left as a free parameter, and adjusted until the 4SIGHT prediction agreed with the field concrete response. Since there were always a number of input parameters that were undetermined, the field validation procedure could only be used to determine if 4SIGHT was unreasonable; the calculation could not be used to validate the program. Although the results of these trials were favorable, they were by no means a validation of 4SIGHT.

The field performance validation concept, which has been used elsewhere [2], is a common approach in service life models for concrete. With few exceptions, these models are empirical and attempt to predict the response of a concrete under certain environmental conditions; they do not attempt to capture every detail of transport and reaction. Some of these models are based on a transport equation such as Fick's law. Others are phenomenological modifications to Fick's law that neglect the details of transport and reaction and seek to simply mimic the macroscopic response of the concrete. Generally, the model parameters are estimated from field data, and then the model is applied to other concretes.

By contrast, the approach of 4SIGHT is to capture every detail of ion transport and chemical reaction. In a sense, the objective is to simulate reality in an attempt to predict future performance. To achieve this, the first step is to fully characterize ion transport and reaction within the concrete. The second is to fully characterize the degradation process, which includes both the effects of reaction on transport properties and the extent of reaction at which sufficient pressures are produced so as to create mechanical failure within the concrete. This approach is virtually unique among concrete service life computer models.

In order to validate the transport portion of the 4SIGHT computer program an inert ceramic frit was used as the model porous material. By using the ceramic frit, the effects of transport could be isolated from the effects of reaction. Further, the results of impedance spectroscopy experiments suggested that the frits contained relatively little surface charge, which would result in relatively little surface binding of the diffusing ionic

species, further contributing to nearly ideal diffusive transport behavior. A practical advantage of the ceramic over cement pastes is that the diffusivity of the ceramic frits was relatively large, meaning that data could be collected over a comparatively short period of time.

The results from the diffusion and the impedance spectroscopy measurements yielded two important facts: the diffusive transport of ionic species within a porous material can be characterized by two numbers, the porosity and the formation factor (defined subsequently), regardless of the number of different diffusing species. The apparent diffusion coefficient that is often reported is of relatively little use, particularly over long periods of time. These two results are significant in that the vast majority of concrete materials transport studies concentrate on the determination of an apparent chloride diffusion coefficient that is calculated from a simplistic transport equation. The fact that formation factor is far more useful has distinct experimental advantage: the formation factor can be determined from an electrical measurement that can be performed by virtually every concrete materials laboratory. Further, the formation factor is a concept that originated in the field of geophysical research. Therefore, it is a technique that should also be familiar to geological testing laboratories.

This report summarizes the experiments that were performed in order to validate the transport portion of the 4SIGHT computer model. Some of the validation consists of comparing the output from 4SIGHT calculations to physical and chemical handbook data for various electrolyte properties. The remaining tests are laboratory experiments performed on the aforementioned ceramic frits. The details of the experiments are published elsewhere, and the results are summarized here.

In addition to the validation, two enhancements to 4SIGHT were requested: a model to predict crack formation within the concrete; and a means to perform a Monte Carlo calculation of the service life based on parameter uncertainty. A model for crack formation was necessary due to the dramatic influence of cracks on advective transport (Darcy flow) through a porous material. The Monte Carlo calculation addresses the nature of uncertainty for any type of service life calculation. No physical parameter can be determined with absolute certainty, and in some cases small variations in a parameter can have a dramatic effect on the overall performance of a structure. The Monte Carlo calculation was implemented with a robust random number generator and permits the user to specify the parameter uncertainty.

The cracking model considered the possible causes of cracks within the concrete and divided the sources of cracking between “engineered” cracks and construction cracks. The engineered cracks (flexural and drying shrinkage) can be reasonably estimated based on the structural design, the materials specification, and the exposure. By contrast, construction cracks (plastic shrinkage, settlement, and thermal) can be avoided by applying proper construction techniques; predicting how well builders will perform their duties is an open-ended question with an indeterminate amount of uncertainty. Hence, the crack prediction was limited to engineering cracks, and are estimated from a simple structural mechanics model (flexural) and the relationships provided in the American Concrete Institute (ACI) *Manual of Concrete Practice* [3] (drying shrinkage).

2 Degradation Validation Examples

The use of either literature data or field data for validating 4SIGHT lacks rigor. In every case, a critical piece of information is missing, which means that some parameter used in the 4SIGHT model remains as an independent parameter. This free parameter can be adjusted until the calculated output from 4SIGHT coincides with the results reported in the literature. If the value chosen for the free parameter is typical for similar concretes, one can only conclude that the 4SIGHT model is *not unreasonable*.

A similar scenario arises with field concretes. For a field concrete that has been in service for decades, many pieces of data are missing. In the rare cases that the construction was documented, many pieces of information required to make accurate estimates of transport properties would not be present. Further, for these concrete structures there are virtually no data of the environmental conditions the concrete had been subjected to over the decades of service.

Another difficulty in the use of field concretes was finding an “old” concrete that had been sufficiently documented, yet was in the appropriate state of degradation. If a concrete structure that was placed in the 1940s degraded after two decades of service, that concrete would no longer exist today. If the same concrete was appropriate for its intended use, it would still be in service today, without any indications of degradation. Old concrete in a measurable state of significant degradation is rare. It was determined that extraction and testing of field concretes would not be cost effective given the rarity of these specimens and the number of unresolved parameters.

The following examples serve as a demonstrations of the types of data available in the literature. Although each example presents all of the relevant data presented in the report, some data are still missing and must be estimated in some way.

2.1 Literature

The task of validating 4SIGHT using published literature required finding suitable reports of concrete performance under various exposures. There are a large number of publications characterizing test specimens and environments. Because 4SIGHT will be used to predict the long term response of concrete, publications dealing with “old” concrete were needed. This fact alone reduced the number of eligible publications dramatically.

An additional complication arises from the state of concrete technology at the time the concrete was produced. Ideally, concretes at least 40 years old would be desirable for this study. The majority of structures having this longevity are typically public projects that consumed large quantities of concrete, the components of which varied over the life of the project, and the properties of which were not characterized thoroughly. This lack of detailed information limits present-day characterization of the concrete. Much of the same can be said for the cements used at the time, for which very little quantitative information exists regarding the cement fineness, oxide composition, and mineral composition. Historical publications such as the Building Science Series [4] published by the U.S. Department of Commerce can only serve as general guides.

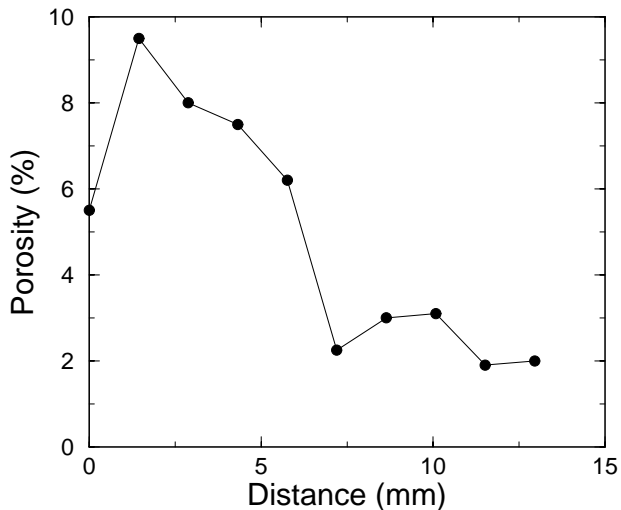


Figure 1: Sample porosity, based upon pores $1\ \mu\text{m}$ to $10\ \mu\text{m}$ in size, as a function of distance from the exposure surface. Graph taken from Trägårdh and Lagerblad [5]

2.1.1 Leaching

In 1906, a drinking water tank was installed in Uppsala, Sweden. The tank was constructed of steel and lined with a concrete mortar. In 1991, the tank was demolished, and the concrete was analyzed by the Swedish Cement and Concrete Research Institute. The results of the analyses were published in an institute report written by Trägårdh and Lagerblad [5].

The water exposure of the concrete provided a nearly constant environment to the concrete. During its service, the tank was periodically drained and filled. There was relatively little evidence of carbonation, suggesting that the specimen analyzed had been submerged for nearly its entire period of service.

Characterization of the concrete is more difficult. No information was given regarding the mixture design. The only characterization the report offered was that the concentration of calcium hydroxide suggested the water-cement ratio might have been approximately 0.40, which would have been quite advanced for that time.

The porosity measurements for pores in the range $1\ \mu\text{m}$ to $10\ \mu\text{m}$ have been reproduced in Fig. 1. These measurements show that the depth of leaching is no greater than 7.5 mm, and that the bulk concrete porosity is 3 % to 4 %. The corresponding bulk paste porosity would be approximately thrice this value, or 9 % to 12 %. Also, the measurements show that porosity near the exposed surface is nearly three times greater than the bulk porosity, which may be due, in part, to the greater paste content near the surface.

Since the chloride diffusion coefficient of the sample was not measured, it had to be estimated. The 4SIGHT prediction is based on a simple model for the diffusion coefficient ($\text{m}^2\cdot\text{s}^{-1}$) that is only a function of water-cement ratio w/c [1]:

$$\log_{10} D_{\text{Cl}^-} = 6.0 w/c - 13.84 \quad (1)$$

Using this equation, the estimated diffusivity for the tank is $3.6 \times 10^{-12}\ \text{m}^2/\text{s}$. This,

along with a water-cement ratio of 0.40, a 0.85 degree of hydration (an assumption in the original 4SIGHT model), and a relation for the porosity ϕ [1],

$$\phi = 1 - \frac{1 + 1.16\alpha}{1 + 3.2w/c} \quad (2)$$

yields an estimate for the capillary porosity of 0.13, which is consistent with the measured values of porosity.

The 4SIGHT program was then used to estimate the porosity. The program started with the following input data file (See Ref. [1] for a description of each parameter):

```
DIFF = 3.6B-12
WC = .40
THICKNESS = 0.100
EXTERNAL Na = 0.00000
EXTERNAL K = 0.00000
EXTERNAL C1 = 0.00000
INTERNAL K = 0.10000
INTERNAL Na = 0.05000
OUTPUT K
OUTPUT Ca
OUTPUT Ca OH
REBAR = .8000
HEAD = 0.0
DEPTH = .2000
JOINT = 0.00000 AT 1.0 UNTIL 100.
CRACK = 0.00000 AT 2.0 DEPTH 0.25
TIME = 33000
```

The diffusivity DIFF is in units of m²/s; the concrete thickness THICKNESS is in units of meters; the INTERNAL and EXTERNAL ion concentrations are in units of moles per liter.

This approach assumes that there were no cracks or joints in the concrete mortar. Also, the REBAR and DEPTH variable were set to large values to eliminate the effects of corrosion or sulfate attack.

The EXTERNAL parameters yield a neutral pH external environment:

Initial state of system:

```
" ION " "EXTERNAL"    "INTERNAL"
"  H:"  0.00000      0.00000
"  Ca:"  0.00000      0.00035
"  Na:"  0.00000      0.05000
"   K:"  0.00000      0.10000
"  OH:"  0.00000      0.15070
"  pH:"  7.00000      13.17810
```

The results using the 4SIGHT estimate for the diffusivity follow:

W/C = 0.40
D = 3.6 E -12

Final System state:

"L(m)"	"porosity"	"pH"	"fc"	"Ca"	"K"	"CaOH"
0.0000	0.1622	7.000	4525	0.0000	0.0000	0.000
0.0050	0.1483	12.404	4747	0.0123	0.0003	39.861
0.0100	0.1345	12.411	4990	0.0119	0.0009	42.963
0.0150	0.1346	12.421	4989	0.0114	0.0017	42.944
0.0200	0.1346	12.431	4988	0.0109	0.0024	42.933

Based upon the values for the porosity and the calcium hydroxide, 4SIGHT predicts that the depth of leaching is between 5 mm and 10 mm. This agrees with the measured values of porosity. However, the porosity near the surface is only a few percent greater than the bulk value of 13.5 %.

A slight modification to the concrete diffusivity yields a marked change in the 4SIGHT estimate:

w/c = 0.40
D = 5.0 E -12

Final System state:

"L(m)"	"porosity"	"pH"	"fc"	"Ca"	"K"	"CaOH"
0.0000	0.4123	7.000	2471	0.0000	0.0000	0.000
0.0050	0.2896	12.400	3456	0.0125	0.0000	9.814
0.0100	0.1670	12.400	4991	0.0125	0.0000	31.971
0.0150	0.1671	12.404	4989	0.0123	0.0003	31.953
0.0200	0.1672	12.408	4988	0.0121	0.0005	31.942

Increasing the concrete diffusivity from 3.6 to 5.0 ($\times 10^{-12}$ m²/s) increased the estimated bulk porosity to 17 %; since the correlation between porosity and diffusivity has considerable uncertainty, it is difficult to assert that one of these estimates is unfounded. The depth of leaching was still between 5 mm and 10 mm. However, the porosity at the surface is now approximately thrice the bulk porosity, as was seen in the published measurements. Although a bulk porosity of 17 % is greater than the measured value, the size limit on the measured capillary pore sizes would suggest that additional capillary porosity would exist in pores smaller than the 1 μ m limit used for the measurements. At best, the values of diffusivity appear to be reasonable upper and lower bounds.

2.1.2 Chloride Diffusion

The Swedish National Testing and Research Institute initiated a research program in which concrete specimens were placed on pontoons in sea water at the Träslövsläge Marine Field Station. Concrete specimens from more than 50 mixture designs ($0.25 \leq w/c \leq 0.75$)

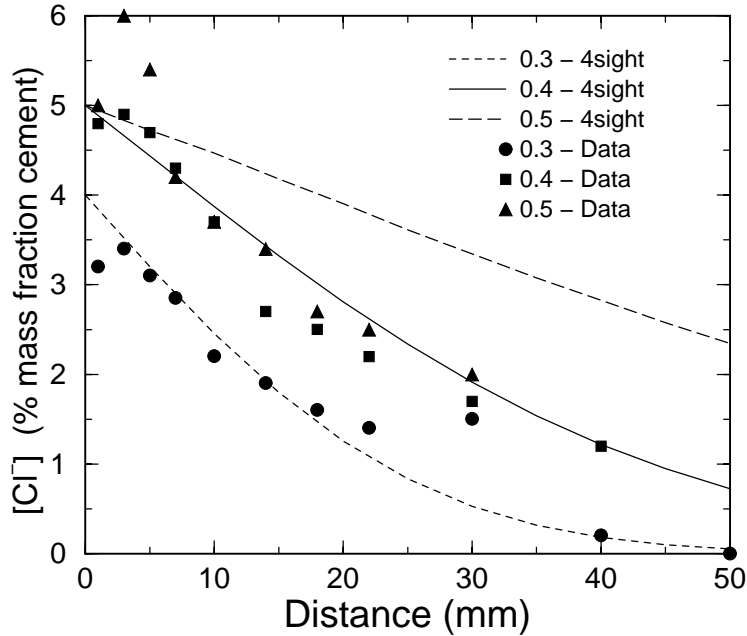


Figure 2: Chloride concentration (percent by mass fraction of cement) for the three concrete mixtures (solid symbols). The concretes are made with ordinary sulfate resistant cements. The curves are estimates by 4SIGHT. Data are reproduced from Sandberg et al. [6].

were arranged in three tiers that define their exposure zone: submerged zone, splash zone, and atmospheric zone. A report of chloride ingress after an exposure of five years was reported by Sandberg, Tang, and Andersen [6]. Samples were extracted from the exposure site and milled, starting from the exposure surface, in 1 mm increments. The material at each depth was analyzed for total chloride content.

The report lists a number of concrete mixtures studied in the program, many of which contain pozzolanic additions. Here, only the results for the ordinary (sulfate resistant) portland cement (SRPC) concrete are considered. The three mixtures are denoted SRPC 0.3, SRPC 0.4, and SRPC 0.5, where the number indicates the water-cement ratio. Also, since 4SIGHT assumes the concrete was continuously saturated, only the data for the submerged exposure are considered.

In the report of Sandberg et al. [6], the chloride ion diffusion coefficient was estimated from the chloride concentration profile within the concrete. These concentration profiles are shown as filled symbols in Fig. 2. It is common that chloride concentrations have a maximum within the concrete, so least squares regression between the solution to Ficks law and the recorded values was applied to the data on the “falling” side of the curve. The results of these regression analyses are shown in Table 1, along with the 4SIGHT predictions for the diffusion coefficient and the paste porosity, based solely upon the water-cement ratio. The curves in Fig. 2 are the 4SIGHT predictions for the chloride concentration, which are based on the estimated diffusion coefficient, not the reported value. The surface chloride concentration for the 4SIGHT estimate was chosen to most

Table 1: Estimated and reported diffusion coefficients, and estimated paste porosities, for the three concrete mixtures considered.

Mixture	4SIGHT		Report
	D_{Cl^-} (10^{-12} m ² /s)	Porosity (paste)	D_{Cl^-} (10^{-12} m ² /s)
SRPC 0.3	0.9	0.04	1.5
SRPC 0.4	3.6	0.14	1.4
SRPC 0.5	14.5	0.22	2.3

reasonably approximate the data; no formal regression was used. Qualitatively, only the estimation for the SRPC 0.3 mixture is accurate. The results for the SRPC 0.4 mixture are reasonable, but not remarkable. The diffusion coefficients from both the 4SIGHT and the Sandberg reports are shown in Table 1. The variation in the diffusion coefficients calculated by regression analysis [6] was less than expected. This is striking given the range in estimated paste porosities.

The reason for the similarity among diffusion coefficients calculated by Sandberg et al. [6] can be explained by the presence of magnesium in the sea water. The magnesium reacts with the available calcium hydroxide to form magnesium hydroxide. The reaction products consume a greater volume than the reactants, and the pores become filled [7]. The greater the quantity of calcium hydroxide, which is proportional to the water-to-cement ratio, the greater is this effect. Since a 0.3 water-cement ratio concrete would have relatively little available calcium hydroxide, the 4SIGHT estimation for this mixture was relatively accurate. This effect also explains why the reported diffusion coefficients for the other concretes were much lower than the 4SIGHT estimates.

2.1.3 HETEK Model

The *Høj kvalitetsbeton-Entreprenørens TEKnologi* (HETEK) {High quality concrete, the Contractors TEChnology} program was initiated by the Danish Road Directorate to establish a system for estimating concrete service life for exposure to marine environments. The entire HETEK program is subdivided into a number of tasks, one of which addresses chloride penetration into concrete. Although HETEK was designed primarily for concrete in marine environments, it would be useful to simply compare the HETEK and the 4SIGHT models.

Since the HETEK program was developed for a specific purpose, the approach to concrete degradation has a focused approach. In a marine environment, cements with reduced sulfate content are specified in order to reduce the reaction of magnesium from within the sea water with sulfate within the cement. The product of this reaction, magnesium sulfate, leads to expansion. An additional effect due to the low sulfate content is that the magnesium is available to react with the calcium hydroxide within the cement paste. The product of this reaction, magnesium hydroxide, has a smaller molar volume than calcium hydroxide, so it does not lead to expansion. Rather, the magnesium hy-

Table 2: The measured diffusion coefficients (D_{HETEK}) and the estimated diffusion coefficient (D_{4SIGHT}) for different values of water-cement ratio (w/c).

w/c	D_{HETEK}	D_{4SIGHT}
0.32	3.9	1.2
0.40	8.5	3.6
0.70	25.1	229.1

droxide seems to “clog” the pore space, effectively reducing the diffusion coefficient of the concrete.

Based upon experimental data, the apparent reduction in the diffusion coefficient due to the magnesium hydroxide is given by the following relationship [2]:

$$\frac{D(t)}{D(t_o)} = \left(\frac{t_o}{t_{\text{ex}} + t} \right)^\beta \quad (3)$$

The quantity t_{ex} is the time at which the concrete was exposed to the marine environment. The quantity t_o is the time at which the concrete diffusion coefficient has reached a steady value, typically 6 months. The parameter β varies from 0.37 to 0.23 for water-cement ratios ranging from 0.30 to 0.75, respectively.

The HETEK model is based upon the solution of Fick’s equation with a time-dependent diffusion coefficient $D(t)$:

$$\frac{\partial c}{\partial t} = D(t) \frac{\partial^2 c}{\partial x^2}$$

The solution to this equation has been published previously [8] for diffusion coefficients having a time dependence as given in Eqn. 3 above. The time dependent behavior for a specific mixture is based upon measurements performed on similar concretes that have had similar exposures. The result is a manual [9] that consists, in large part, of nomographs for the estimation of concrete service life, defined as the time until failure due to corrosion of the steel reinforcement.

To develop the analytical equations for the time-dependent diffusion coefficient, the researchers required large quantities of diffusion data. Only a fraction of these data are shown in the reports. As a basic check, a comparison of the measured diffusion coefficients with the estimates by 4SIGHT based upon the water-cement ratio is given in Table 2. The estimates for the 0.32 and the 0.40 water-cement ratio concretes are within an order of magnitude of the HETEK values. This is encouraging given the single datum, w/c, used for the estimate. The 4SIGHT estimate for the 0.70 water-cement ratio concrete differs by an order of magnitude. Fortunately, 0.70 water-cement ratio concretes are undesirable for structures designed to inhibit advective and diffusive flow.

3 Transport

Validating the transport model within 4SIGHT is paramount to validating its estimate of service life. Every degradation mechanism considered by 4SIGHT depends on the transport of ionic species through the concrete. Therefore, a proper validation requires that the transport model is sufficiently comprehensive in order that it can predict the behavior of electrolytic solutions.

The first characteristic of electrolytic solutions to be considered is the coulomb interactions among the diffusing ionic species. To account for ion-ion interactions one must determine how the ions would respond to charge imbalances. The solution is the electro-diffusion equation, which has been used extensively in solid state physics [10], the biological sciences [11, 12], and only recently in the concrete materials research [13–16].

The second characteristic is due to changes in the solution due to changes in species chemical activity. Since the pore solution of cement paste typically has an ionic strength of approximately 0.5 mol/kg, one must also account for the nonideal diffusive behavior of each species. This nonideal behavior is related to excluded volume and the second virial coefficient. This effect is quantified through the chemical activity of the species. The chemical activity a of a species can be related to the ionic concentration c through the mathematical construct of an activity coefficient γ :

$$a = \gamma c \tag{4}$$

The value of the activity coefficient, a dimensionless number between zero and one, depends on the concentration and units used for the concentration: mol/L, mol/kg, mol/m³, etc. Although there are a number of approximation schemes for calculating the activity coefficient, the Pitzer equations [17] were used in 4SIGHT since relevant coefficients are readily available and the resulting estimate is accurate over the range of ionic strengths typically found in cement paste pore solution.

The combination of the electrostatic interactions and the activity coefficient calculation yielded a robust transport equation. The electro-diffusion equation can be used to predict the single diffusion coefficient for a binary salt, which are reported in chemistry reference handbooks, over a range of concentrations, demonstrating the concentration dependence on the apparent diffusion coefficient.

3.1 Transport Equation

The pore solution of hardened cement paste has an ionic strength of approximately 0.5 mol/kg. At this ionic strength, the pore solution cannot be modeled using equations that characterize idealized transport, which generally treat each ionic species independently of one another. Further, regardless of the ionic strength, the electrostatic interactions among the various species are quite strong. Although the self-diffusion coefficient for sodium ions is smaller than that of chloride ions, the electrostatic interactions enforce electro-neutrality, and the two ions diffuse with the same apparent self-diffusion coefficient, giving a diffusion coefficient for the salt; these diffusion coefficients are reported in chemistry reference handbooks.

Further, the chemistry handbooks report the salt diffusion coefficient as a function of concentration. The electrostatic interactions, by themselves, are insufficient to characterize this phenomenon. One approach to capture this behavior in a transport model is to use self-diffusion coefficients that are a function of concentration. However, the concentration dependence of sodium chloride is not the same as for magnesium chloride. Therefore, some experimenters have used empirical relations to predict diffusion coefficients based on both concentration and speciation [18]. This approach, however, can only be used to interpolate results; any new species, or concentrations outside the range from which the coefficients were determined, would invalidate the result.

The alternative approach is to characterize the ion-ion interactions at a fundamental level, thereby “calculating” the effects of concentration and speciation. The electrostatic interactions give rise to an electrical field that ensures electro-neutrality. This field is unique and can be calculated using principles of electrostatics. The macroscopic effect of the electrostatic interactions is an electrical potential (the diffusion potential) that exists across the specimen, and is measurable.

The concentration dependence arises from mechanical ion-ion interactions that only manifest themselves at elevated concentrations. The presence of a concentrated ionic species acts to change the hydrodynamic properties of the electrolyte, thereby changing the apparent viscosity of the fluid. This behavior is related to the species activity, which is a function of its chemical potential.

3.1.1 Electrical Measurements

Before discussing the transport equation, it will be useful to consider the relationship between conductivity and diffusivity. These principles are fundamental to the final expression of the transport equation. The final form exploits the formation factor, which is a material parameter that can be determined directly from conductivity measurements.

Conductivity measurements hold great promise for estimating the formation factor of saturated porous materials. The two most commonly used conduction techniques are the electrical migration test (driven diffusion) and the conductivity measurement. Migration tests are used to determine the ionic mobility, which can be related to diffusivity. Conduction tests are used to estimate the formation factor, which can also be related to diffusivity. While there have been many reports on the use of the electrical migration tests to determine the diffusion coefficient of cementitious systems [19], there have been fewer reports on the use of the formation factor. This is unfortunate, since the formation factor is directly related to the diffusivity of the material pore structure. The relationship between formation factor and diffusivity, however, has subtleties that must be considered when making estimates of one from the other.

The formation factor F has its origin in geological research on saturated porous materials. For a nonconducting porous solid saturated with a conducting pore solution, the formation factor is the ratio of the pore solution conductivity σ_p to the bulk conductivity σ_b [20]:

$$F = \frac{\sigma_p}{\sigma_b} \quad (5)$$

This quantity characterizes the solid microstructure since the only difference between the

conductivities is due to the restricted pathways through which the current is constrained in the bulk conductivity measurement.

The use of conduction tests to estimate the diffusion coefficient is due to the relationship between conductivity and diffusivity. In an electrolytic solution, the contribution an ionic species makes to the overall conductivity can be expressed as a function of its conventional (electrochemical) mobility u , amount-of-substance concentration c , and valence z [21]:

$$\sigma = z c \mathcal{F} u \quad (6)$$

The quantity \mathcal{F} is the Faraday constant. The mobility can then be related to diffusivity through the Einstein relation [21]:

$$z \mathcal{F} D = R T u \quad (7)$$

The quantity R is the universal gas constant and T is the absolute temperature. Using these equations, one can estimate the diffusion coefficient from either measurements of ion mobility (driven diffusion) or from the conductivity contribution of a particular ion (conductivity).

Alternatively, if a porous material is saturated with a dilute electrolytic solution, the ratio of the pore solution conductivity σ_p to the bulk conductivity σ_b would be equal to the ratio of the diffusion coefficient of an ion in the pore solution D_p to the bulk diffusion coefficient D_b of that ion:

$$F = \frac{\sigma_p}{\sigma_b} = \frac{D_p}{D_b} \quad (8)$$

Note that this relationship holds even if the Einstein relation is incorrect at large concentrations; the multiplicative error occurring in both D_p and D_b would cancel. Since the self-diffusion coefficient of ions can be found in books, this is a provocative approach to determining the bulk diffusion coefficient D_b [22].

Unfortunately, the pore solution of typical cementitious systems can have a large ionic strength ($0.5 \text{ mol}\cdot\text{kg}^{-1}$ to $1.0 \text{ mol}\cdot\text{kg}^{-1}$), and so care must be exercised when estimating the bulk diffusion coefficient from the formation factor. At these large ionic strengths, the pore solution diffusion coefficient D_p of an ion is different from the self-diffusion coefficient, which is the value reported in tables [23]. Equation 8 can still be used, if one can correctly determine the diffusion coefficient D_p in the pore solution. Unfortunately, given the constraints of most experimental diffusion apparatus, and that experimenters typically measure time dependent concentrations, an exact value for D_p can be difficult to define.

An alternative approach is to determine the formation factor from the diffusion data by separating the microstructural dependence from the concentration dependence in the diffusion coefficient. It will be shown that the formation factor can be alternatively expressed as a function of the *microstructural* diffusion coefficient of the porous material. The microstructural diffusion coefficient is independent of both changes in the pore solution chemistry and the diffusion potential. The estimated formation factor could then be used to estimate the diffusive transport of any ion within the studied system since it uniquely characterizes the solid pore structure; the chemical effects would be calculated independently.

3.1.2 Diffusive Ionic Flux

The proper application of the formation factor to porous systems containing concentrated electrolytes can be best studied by starting with the appropriate transport equation. For the case of diffusing charged species in concentrated electrolytes, the transport is governed by coupled electrical and diffusive transport, and ion-ion interactions must be also be considered.

The diffusion of ionic species in an electrolyte is governed by the electro-diffusion equation. For the i -th ionic species, the electro-diffusion equation relates the bulk flux \mathbf{j} to the concentration c , the diffusion potential ψ_D , the bulk microstructural diffusion coefficient D_μ , and the bulk conventional mobility u [10]:

$$\mathbf{j} = -D_\mu \left(1 + \frac{\partial \ln \gamma}{\partial \ln c} \right) \nabla c - z \mathcal{F} u c \nabla \psi_D \quad (9)$$

The subscript i has been omitted here in order to improve visual clarity of the equation, and will be added later. The quantity γ is the activity coefficient for the species. Although this equation neglects adsorption effects, it is otherwise a complete description of the nonreacting diffusive transport of charged species in concentrated electrolytes. Equation 9 still bears a resemblance to Fick's law for apparent diffusion D_a [24]:

$$\mathbf{j} = -D_a \nabla c \quad (10)$$

The quantity $D_\mu[1 + \partial \ln \gamma / \partial \ln c]$ is an *agglomerated* diffusion coefficient that includes the effects of changes in both the microstructure and the concentration.

It should be noted that the *agglomerated* diffusion coefficient is not the *apparent* bulk diffusion coefficient D_b . Strictly speaking, the apparent diffusion coefficient also includes the effects of the diffusion potential ψ_D . In those cases where the self-diffusion coefficients of all the diffusing species are nearly identical, the diffusion potential will be nearly zero, and the apparent diffusion coefficient will be nearly equal to the agglomerated diffusion coefficient. However, for cementitious systems, there are many species present with varying self-diffusion coefficients.

Ideally, one would like to distinguish between the effects due to microstructural changes and the effects due to changes in the pore solution electro-chemistry. By observation, one can see that the microstructural diffusion coefficient D_μ characterizes the solid microstructure and that the quantity in parenthesis characterizes the pore solution chemistry. The microstructural diffusion coefficient is itself independent of the pore solution chemistry. A demonstration of how to extract the value of microstructural diffusion coefficient from a diffusion experiment is accomplished through a detailed discussion of the formation factor.

3.1.3 Formation Factor

Consider an electrical measurement of the formation factor F performed on a porous specimen saturated with a concentrated electrolyte. The conductivity of the pore solution σ_p is a function of the ionic strength I . The conductivity is proportional to the ionic strength such that as the ionic strength approaches a value of zero, the conductivity also

approaches a value of zero. Similarly, the bulk conductivity has the same dependence on the pore solution conductivity. If the pore solution conductivity doubles, the bulk conductivity will also double, ignoring surface conduction contributions.

The diffusion coefficient of an ion in a concentrated electrolyte has a different type of dependence on the ionic strength. The self-diffusion coefficients reported in tables are limiting values under the condition that the limit that both the concentration and the diffusion potential go to zero. In the practical dilute limit, the cations and the anions of a 1:1 valence electrolyte must diffuse together due to charge neutrality. This leads to the creation of the diffusion potential. Therefore, the pore solution diffusion coefficient D_p must be an function of the ionic strength, activity coefficients, and the diffusion potential:

$$D_p = D^s [1 + g(I, \gamma, \psi_D)] \quad (11)$$

The function g is an arbitrarily complex function of the ionic strength I , the activity coefficient γ , and the diffusion potential ψ_D . It characterizes the interaction between diffusion ionic species and the bulk electrolyte. The quantity D^s is the self-diffusion coefficient reported in tables [23]. A similar relationship characterizes the bulk diffusion coefficient D_b :

$$D_b = D_\mu [1 + g(I, \gamma, \psi_D)] \quad (12)$$

The function g is the same since the diffusion ionic species will see the same electrolyte. The microstructural diffusivity D_μ is the value corresponding to the dilute limit for the bulk diffusivity. It is independent of both the activity coefficient and the diffusion potential, and is the same quantity that appears in Eqn. 9.

Using these relations, the formation factor can be written as a function of quantities that are themselves functions of the ionic strength I , activity coefficient γ , and the diffusion potential ψ_D :

$$F = \frac{\sigma_p(I)}{\sigma_b(I)} = \frac{D^s [1 + g(I, \gamma, \psi_D)]}{D_\mu [1 + g(I, \gamma, \psi_D)]} = \frac{D^s}{D_\mu} \quad (13)$$

However, the resulting formation factor F is independent of both the ionic strength and the ionic species; a fact that is exploited by numerical calculations of formation factor on model microstructures [25].

The advantage of using the ratio D^s/D_μ is not immediately obvious. In Eqn. 8, D_b is observable, but D_p is difficult to determine precisely in typical diffusion experiments containing a variety of species, each with varying concentration. In Eqn. 13, D^s can be found in tables, but the quantity D_μ cannot be observed in electrolytes because the effects of the diffusion potential cannot be eliminated. Serendipitously, the usefulness of D_μ in service life prediction through its use in the electro-diffusion equation is also the key to determining this quantity from experiment.

The formation factor is extremely useful in models of ionic transport. Accurate service life predictions require models that can account for independent changes in either the solid microstructure or the pore solution chemistry. A suitable computer program could solve the electro-diffusion transport equation by using estimates of the ion activity coefficient γ from published empirical relations and using the local electro-neutrality condition to solve

for the diffusion potential. The microstructural diffusion coefficient D_μ in the electrodiffusion equation would be calculated from the formation factor F and the dilute limit self diffusion coefficient D^s :

$$D_\mu = \frac{D^s}{F} \quad (14)$$

Note that this relation holds for all the species, yet there is only a single value for the formation factor F .

Alternatively, one can determine the formation factor from experimental diffusion data by using the same computer program. Using a computer program that implements Eqns. 9 and 14, one adjusts the formation factor until the computed output matches the experimentally observed quantities. The experimental program described subsequently used this approach to determine the formation factor from divided cell diffusion measurements.

3.1.4 Conservation Equation

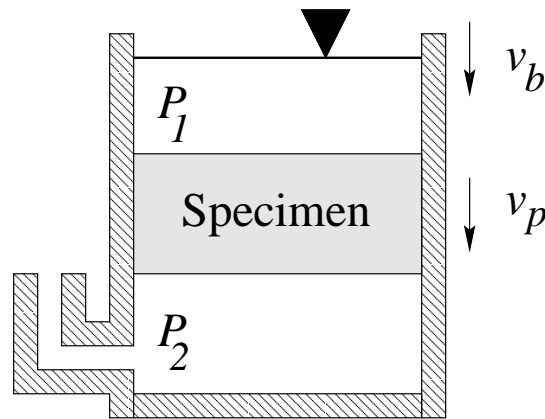


Figure 3: Schematic of the bulk flux and the pore flux, characterized by the bulk velocity \mathbf{v}_b and pore velocity \mathbf{v}_p , due to a pressure hydrostatic pressure drop of $P_1 - P_2$ across the specimen.

The flux in Eqn. 9 was developed for transport within an electrolyte. Transport through a porous material must account for the solid framework that comprises the material. The schematic of the Darcy experiment shown in Fig. 3 demonstrates the difference between the pore flux (through electrolyte) and bulk flux (through porous material).

The experiment shown in Fig. 3 includes a porous specimen saturated with a brine. The volumes above and below the specimen are filled with the same brine. Due to a hydrostatic pressure P_1 applied above the sample, there is a mass flow of the brine through the porous specimen. The top free surface of fluid “falls” at a velocity of \mathbf{v}_b ,

representing the bulk velocity of the fluid through the sample. If the fluid above the sample were instantaneously filled with a colored dye, the “front” of the dye would advance through the specimen at the pore velocity \mathbf{v}_p . The pore flux \mathbf{j}_p of ionic species within the brine would be proportional to the species concentration c : $\mathbf{j}_p = c\mathbf{v}_p$. Similarly for the bulk flux: $\mathbf{j}_b = c\mathbf{v}_b$.

Employing conservation of mass, and assuming that water is incompressible at these pressures, the pore velocity \mathbf{v}_p will be greater than the bulk velocity \mathbf{v}_b . The ratio of the velocities is the connected porosity ϕ : $\mathbf{v}_b = \phi\mathbf{v}_p$. The porosity is also the ratio of the pore area and the bulk area: $A_p = \phi A_b$. Likewise, by conservation of ionic species, the rate at which species are transported through the system is the same above, inside, and below the specimen:

$$\mathbf{j}_b A_b = \mathbf{j}_p A_p \quad (15)$$

$$\mathbf{j}_b = \phi \mathbf{j}_p \quad (16)$$

This is an important relationship when considering diffusive and advective transport through porous media. With a relationship between the pore flux \mathbf{j}_p and the bulk flux \mathbf{j}_b , one can now develop the appropriate flux relationships for each of the three transport mechanisms (diffusion, permeation, and conduction) considered in 4SIGHT.

As mentioned previously, the hydrodynamic flux will occur due to Darcy flow under a hydraulic pressure gradient ∇P across the specimen. The bulk velocity \mathbf{v}_b is equivalent to the Darcy velocity:

$$\mathbf{v}_b = \frac{-k_b}{\mu} \nabla P \quad (17)$$

This result, and the similar one for the pore velocity, can be substituted into the appropriate flux equation:

$$\mathbf{j}_b = c\mathbf{v}_b = \frac{-ck_b}{\mu} \nabla P \quad (18)$$

$$\mathbf{j}_p = c\mathbf{v}_p = \frac{-ck_p}{\mu} \nabla P \quad (19)$$

$$k_b = \phi k_p \quad (20)$$

In nearly every application of Darcy’s law to concrete, researchers report the bulk permeability k_b , so the bulk flux \mathbf{j}_b is most convenient.

Although it has been argued that the electro-diffusion equation is a more complete description of diffusive transport, the simplified Fick’s law is used here as a demonstration of the distinction between pore flux and bulk flux:

$$\mathbf{j}_b = -D_b \nabla c \quad (21)$$

$$\mathbf{j}_p = -D_p \nabla c \quad (22)$$

$$D_b = \phi D_p \quad (23)$$

Reported results from diffusion measurements vary between reporting either the pore flux \mathbf{j}_p or the bulk flux \mathbf{j}_b . Unfortunately, this distinction is not always made, and so the reader must exercise care when interpreting the results from diffusion experiments.

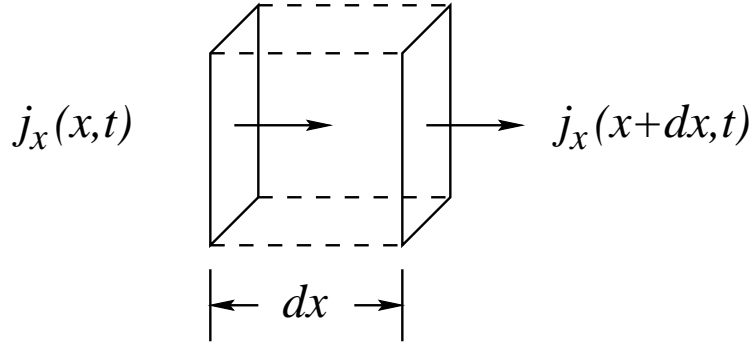


Figure 4: Schematic for ionic flux conservation through a volume of unit area and differential width dx .

The conductive flux is that which occurs due to the application of an electrical field. Strictly speaking, the flux is proportional to the conventional ionic mobility u . The pore flux and bulk flux depend on the corresponding pore and bulk mobilities:

$$\mathbf{j}_b = -zc\mathcal{F}u_b\nabla\psi \quad (24)$$

$$\mathbf{j}_p = -zc\mathcal{F}u_p\nabla\psi \quad (25)$$

$$u_b = \phi u_p \quad (26)$$

In general, the mobilities are approximated using the Einstein relation:

$$u = \frac{D}{RT} \quad (27)$$

The diffusion coefficient D is the self-diffusion coefficient reported in tables [23]. This relationship, however, is only valid in the dilute limit.

With the pore and bulk flux equations established for both diffusion and conduction transport, a time-dependent equation is needed in order to calculate changes in concentration. This equation can be derived from the conservation of species. Figure 4 shows a volume element with unit area and differential width dx . The x -component of the species flux entering the volume is $j_x(x, t)$, and the flux exiting is $j_x(x + dx, t)$. The rate, per unit area, at which species are filling the volume is $j_x(x, t) - j_x(x + dx, t)$. The change in the concentration is this difference divided by the width dx :

$$\frac{\partial c}{\partial t} = \frac{j_x(x, t) - j_x(x + dx, t)}{dx} = \frac{-\partial j_x}{\partial x}$$

$$\frac{\partial c}{\partial t} = -\nabla \cdot \mathbf{j} \quad (28)$$

Now this equation must be reformulated to account for a porous material.

The equation for a porous material can be obtained from the definition of concentration. The experimentally useful quantity is the intrinsic, or pore concentration c , in units of moles of species per unit pore volume V_p . Let the bulk concentration \bar{c} represent

the number moles per unit bulk volume V_b (volume of pore solution and solid structure combined). Apply Gauss's divergence theorem to Eqn. 28 over the bulk volume V_b :

$$\int \frac{\partial \bar{c}}{\partial t} dV_b = - \int \nabla \cdot \mathbf{j}_b dV_b \quad (29)$$

The bulk concentration \bar{c} can be related to the intrinsic concentration through the porosity: $\bar{c} = \phi c$. The resulting conservation equation relates the bulk flux \mathbf{j}_b to the intrinsic concentration c :

$$\frac{\partial \phi c}{\partial t} = -\nabla \cdot \mathbf{j}_b \quad (30)$$

$$\frac{\partial \phi c}{\partial t} = -\nabla \cdot \phi \mathbf{j}_p \quad (31)$$

These relationships have been published elsewhere [26–29], primarily in the field of geophysical research.

3.1.5 Complete Transport Equation

The complete transport equation has separate terms for the diffusion, conduction, and permeation components of the flux. Substituting for the bulk microstructural diffusion D_μ , the self-diffusion coefficient D_i^s , the formation factor F , and the definition of the Darcy velocity \mathbf{v}_b yields the following time-dependent transport equation.

$$\begin{aligned} \frac{\partial \phi c_i}{\partial t} &= -\nabla \cdot \mathbf{j}_{b,i} \\ &= \frac{D_i^s}{F} \nabla \cdot \left(1 + \frac{\partial \ln \gamma_i}{\partial \ln c_i} \right) \nabla c_i + \frac{z_i \mathcal{F}}{RT} \frac{D_i^s}{F} \nabla \cdot c_i \nabla \psi_D + \nabla \cdot \frac{k_b c_i}{\mu} \nabla P \end{aligned} \quad (32)$$

This transport equation is significant in that only three numbers (ϕ , F , k_b) are required in order to characterize the transport of an arbitrary number of ionic species.

4 Transport Validation

Validation of the transport equation within 4SIGHT is a two-stage process. First, 4SIGHT will be used to calculate the properties of bulk fluids. These properties include density, activity coefficient, and salt diffusion coefficient. These results can then be compared to values reported in chemistry handbooks. Second, 4SIGHT will be used to calculate the response of a controlled diffusion experiment performed on a well-defined porous material. The porous material is nonreactive and has relatively little surface charge.

4.1 Reference Data

Comparisons between 4SIGHT and reference data are needed in order to ensure that the fundamental building blocks of 4SIGHT are constructed in an orderly manner. Practical field data are nearly always reported in units of molarity (mol/L), or similar units of quantity per volume. The calculation of the activity coefficient, however, is based on concentration expressed in units of molality (mol/kg). Converting between molarity and molality, requires an estimate of the solution density. From a coherent means of calculating density and activity coefficient, one can then use the electro-diffusion equation to calculate the diffusion coefficient of various binary salts and compare the results to values reported in chemistry handbooks.

4.1.1 Electrolyte Density

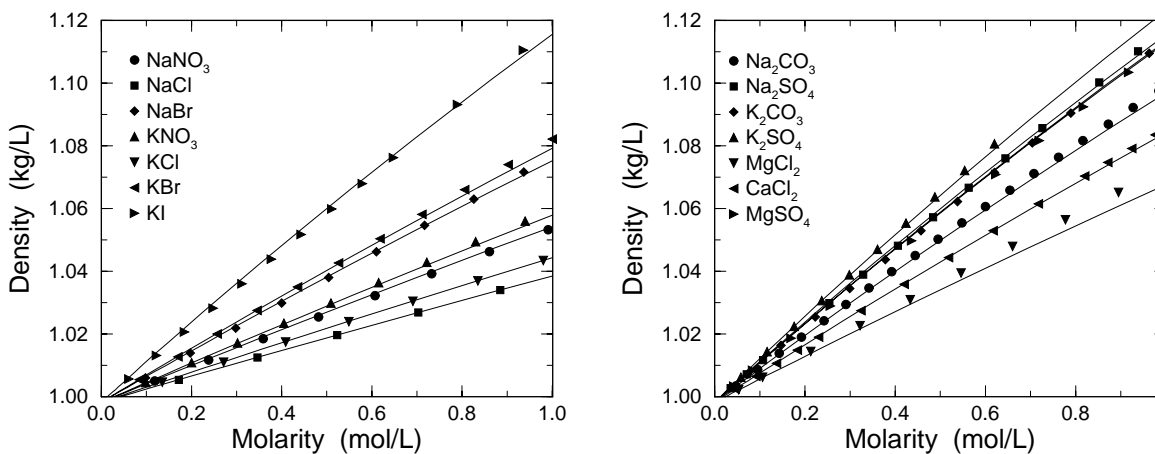


Figure 5: Density of 1-1 electrolytes (a) and 1-2, 2-1, and 2-2 electrolytes (b) as a function of molarity. Data from the chemistry handbook appear as symbols. The predictions by 4SIGHT appear as solid curves.

A review of approximation schemes for various electrolyte properties revealed no established means of estimating the electrolyte density. The scheme implemented by

4SIGHT was to assume that each ionic species contributes independently to the overall density. The contribution is a function of the density and the mole fraction of that species within the electrolyte.

In Figs. 5a and 5b are the results for nominally pH neutral salts. The density is shown as a function of electrolyte concentration. The estimates of 4SIGHT are denoted by solid curves. The data from the CRC Handbook [30] are denoted by filled symbols. The results for the 1-1 electrolytes are shown in Fig. 5(a), and those for the 1-2, 2-1, and 2-2 electrolytes are shown in Fig. 5(b). In both cases, the approximations are relatively accurate over the full range of concentrations. In general, the accuracy for the 1:1 salts are better than for the 1-2 and 2-1 salts. For both cases, the accuracy is well within one percent over the concentration range shown.

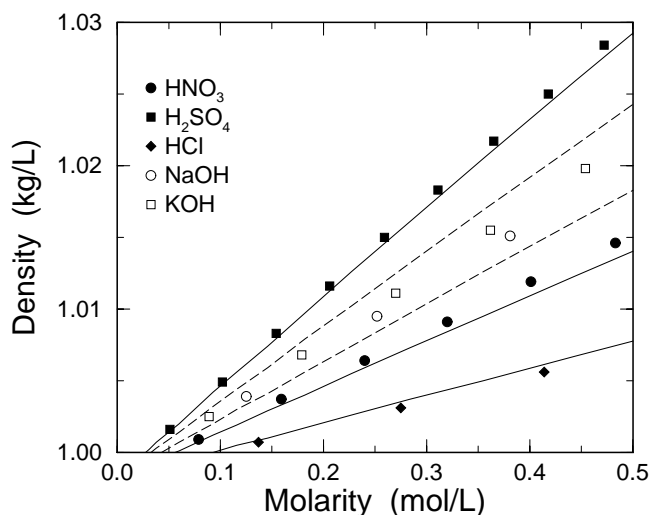


Figure 6: Density of strong acids and bases. Data from the chemistry handbook appear as symbols. The predictions by 4SIGHT appear as solid curves.

The density estimates for strong acids and bases are shown in Fig. 6 as a function of electrolyte concentration. The estimates by 4SIGHT are denoted by solid curves. The handbook values for acids are denoted by filled symbols, and values for bases are denoted by open symbols. Generally, the results for acids and bases are not as accurate as for the pH neutral salts. Nevertheless, the accuracy is still less than a percent over the concentration range shown.

4.1.2 Activity Coefficient

Accurate estimates of activity coefficients are necessary for both calculations of transport flux at elevated concentrations and for calculations of equilibrium species concentrations in reacting systems. In 4SIGHT, the activity coefficient is calculated using the equations of Pitzer [17]. To reduce complexity and gain computational speed, a “truncated” implementation was used. All interactions composed of two and three charged species were implemented; all other interactions were been omitted.

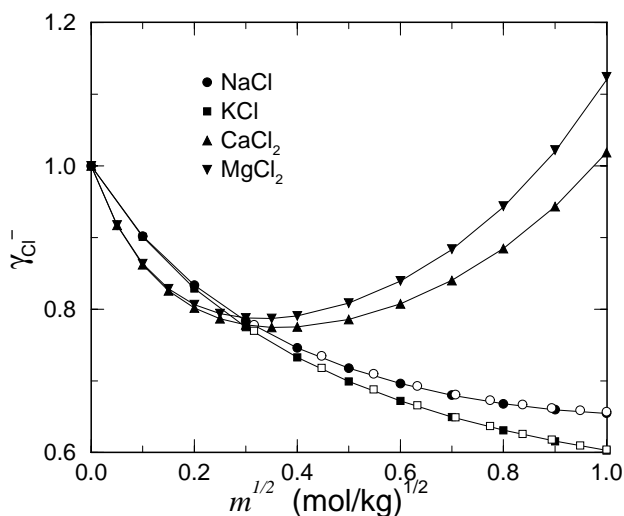


Figure 7: Activity coefficient of chloride ions γ_{Cl^-} as a function of molality m for various electrolytes. The estimates by 4SIGHT are shown as solid curves. Results from the PHRQPITZ computer program [31] are shown as filled symbols. Data from the *CRC Handbook of Chemistry and Physics* [30] are shown as open symbols.

As a measure of performance, the results from 4SIGHT are compared to both CRC Handbook data and the results of the PHRQPITZ [31] computer program, which is a full implementation. Shown in Fig. 7 are the results for the activity coefficient of chloride ions γ_{Cl^-} as a function of electrolyte concentration. The estimates by 4SIGHT are denoted by solid curves. The values from PHRQPITZ are denoted by filled symbols, and the values from the CRC Handbook are denoted by open symbols. Generally, the agreement among all three is very good over the entire range of electrolyte concentration shown, suggesting that the 4SIGHT implementation is sufficient. This example of chloride ion activity is characteristic of the accuracy with which 4SIGHT can estimate the activity of all the ionic species incorporated into the program.

4.1.3 Electrolyte Diffusion Coefficient

The electrolyte diffusion coefficient was calculated by 4SIGHT and compared to values published in the CRC Handbook. The “sample” had a porosity of one, and a formation factor of one. The change in concentration across the specimen was only a few percent. The flux of salt passing through the solution was then used to calculate an apparent diffusion coefficient, based on Fick’s law (Eqn. 10). This apparent diffusion coefficient was then compared with the handbook value.

Data for various electrolytic solutions are shown in Table 3 over varying concentrations. Generally, 4SIGHT is accurate to within a few percent up to 0.1 mol/L. The error increases with concentration and is greater for larger valence species. The results are still reasonable, considering that a species with a 1.0 mol/L concentration within concrete pore solution is relatively rare.

Table 3: Comparison of diffusion coefficients D from the computer program (CP) and handbook (HB) (Ref. [30]) values for various salts in aqueous solution.

Salt	conc. mol·L ⁻¹	D_{HB} 10 ⁻⁹ m ² ·s ⁻¹	D_{CP} 10 ⁻⁹ m ² ·s ⁻¹	$\frac{D_{CP}-D_{HB}}{D_{HB}}$
KCl	0.01	1.917	1.902	-0.0078
	0.10	1.844	1.807	-0.0201
	1.00	1.892	1.801	-0.0481
NaCl	0.01	1.545	1.539	-0.0039
	0.10	1.483	1.476	-0.0047
	1.00	1.484	1.571	+0.0586
LiCl	0.01	1.312	1.307	-0.0038
	0.10	1.269	1.277	+0.0063
	1.00	1.302	1.555	+0.1943
LiBr	0.10	1.279	1.286	+0.0055
	1.00	1.404	1.647	+0.1731
LiNO ₃	0.01	1.276	1.277	+0.0008
	0.10	1.240	1.242	+0.0016
	1.00	1.293	1.467	+0.1346
KNO ₃	0.01	1.846	1.831	-0.0081
KI	0.10	1.865	1.829	-0.0193
	1.00	2.065	1.911	-0.0746
Na ₂ SO ₄	0.01	1.123	1.059	-0.0570
MgSO ₄	0.01	0.710	0.568	-0.2000

The result for MgSO₄ is rather anomalous. The value calculated by 4SIGHT is consistent with the approximation based on the Nernst relation:

$$D = (z_+ + z_-) \frac{D_+ D_-}{z_+ D_+ + z_- D_-} \left(1 + \frac{\partial \ln \gamma_{\pm}}{\partial \ln c} \right) \quad (33)$$

The values calculated by 4SIGHT are consistent with this equation, as are many of the handbook values. The discrepancy in the MgSO₄ result may be due to either experimental errors in the handbook value or the use of the Einstein relation in Eqn. 7 as an approximation for the ionic mobility u . A more rigorous estimate would require a concerted effort to develop an estimate of the ionic mobility as a function of concentration.

4.2 Laboratory Data

The laboratory experiments were performed in two stages. The first stage validates the use of the formation factor in the transport equation. Independent electrical measurements of formation factor are compared with values estimated from diffusion data. The second stage consists of a series of diffusion measurements that attempts to demonstrate

that the transport equation is valid for a range of ionic species. Further, the varied behavior of these electrolytes was used to demonstrate that the apparent bulk diffusion coefficient depends strongly on the species present, and comparatively weakly on the ionic strength, over the range of concentrations that are of interest.

Results from the two stages of experiments have been presented [32,33] and submitted for publication [34,35]. The experimental details and the results are repeated here for completeness.

4.2.1 Ceramic Frit

The diffusion experiments were performed on a commercial porous frit composed of a sintered alumina ceramic (99.8 % alumina) measuring (50.76 ± 0.04) mm in diameter and (6.48 ± 0.03) mm thick; the uncertainty is an estimated standard deviation calculated from 7 frits. Mercury intrusion porosimetry analysis revealed a porosity of approximately 0.26, and a pore size distribution concentrated between 350 nm and 450 nm. This is consistent with the manufacturer’s published specification of a pore size less than 500 nm.

The alumina frit was regarded as a nearly ideal porous medium for studying diffusive transport. The alumina is chemically stable at moderate values of pH. In addition, conductivity measurements suggest that the frit has a relatively low bound surface charge. As defined in Eqn. 5, the formation factor F is calculated from the ratio of the pore fluid electrical conductivity σ_p to the the bulk electrical conductivity σ_b with that pore fluid. The calculation can be repeated for different pore solutions with varying values of σ_p .

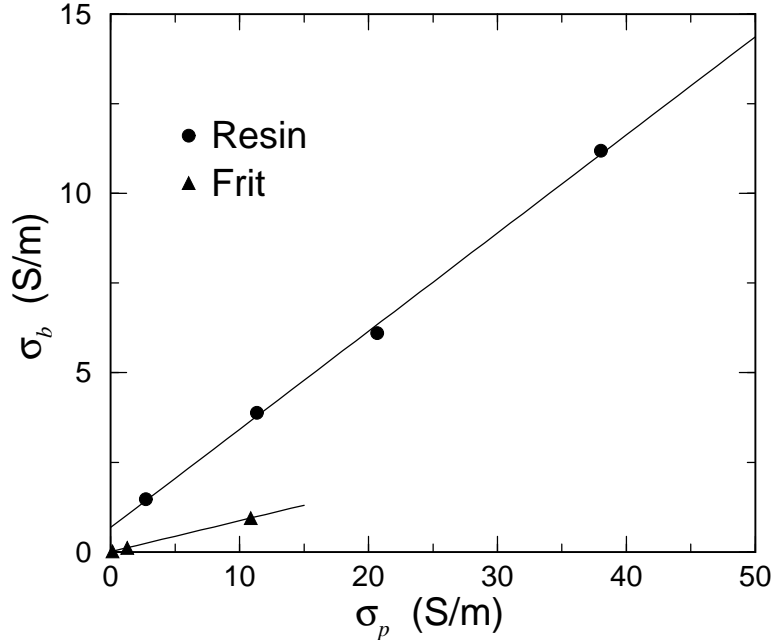


Figure 8: The pore solution conductivity σ_p and the corresponding bulk conductivity σ_b for the resin system of McDuff and Ellis [36] and the frit system used here.

Such an experiment was performed in 1979 by McDuff and Ellis [36] on a model porous material composed of a packed column of cation exchange resin. Their data for large

pore solution conductivities are denoted in Fig. 8 by filled circles. Linear ordinary least squares regression applied to the data reveal a positive intercept of (0.68 ± 0.17) S/m; the uncertainty is an estimated standard deviation. Similarly, one of the frits was saturated with standard potassium chloride conductivity solutions [37], and the data are also shown in Fig. 8 as filled triangles. For the frit, the intercept was only (0.00258 ± 0.00025) S/m. Because the intercept is proportional to the surface charge of the material [38], one expects that the surface charge of the frit is approximately 250 times smaller than that of the resin. Unfortunately, comparisons with cementitious systems are not possible due to lack of similar data. Regardless, the data presented herein for the frit system will show that an analysis that neglects binding still captures all the salient features of the effect that speciation has on the diffusive transport of ions through these ceramic frits.

4.2.2 Experimental Setup

The divided cell arrangement was used as the experimental apparatus because of its procedural simplicity. Since the ceramic specimens have a relatively large diffusion coefficient, compared to hydrated cement paste, usable data could be collected in a reasonable period of time. As mentioned previously, the ceramic material also has a relatively small surface charge and surface adsorption effects could be neglected. The result is a material that should exhibit nearly ideal diffusive transport properties.

The target ion for the experiment was iodide. The iodide concentration was determined using a commercial solid-state ion selective combination electrode. Iodide was chosen as the target ion because of experimental advantages iodide electrodes have over chloride electrodes. For each measurement, the electrode was standardized using reference iodide solutions.

Each ceramic frit was first mounted, using epoxy, into an acrylic annulus. After the epoxy had cured, the specimen was saturated with a potassium iodide solution under vacuum. The saturated frit was then clamped between two glass vessels, each having a capacity of approximately 250 mL, using rubber o-rings for a water tight seal. One vessel was filled with KI and the other with a test electrolyte. Both vessels were sealed to reduce evaporation, and then placed inside a walk-in environmental chamber maintained at 25 °C. All sampling and concentration measurements were performed within the chamber in order to ensure stability in both the diffusion and the measurements; there is a nominal 2 %/°C variation in the self-diffusion coefficient [23].

4.2.3 Analysis

Historically, ionic transport in cementitious systems has been characterized by Fick’s law of diffusive transport:

$$\mathbf{j}_i = -D_i^a \nabla c_i \tag{34}$$

The quantity D_i^a represents an *apparent* diffusion coefficient for the i -th species. The analysis of the experimental diffusion data is based on the “constant gradient” assumption that underlies Fick’s law. Based on this assumption, the concentration gradient across the specimen is constant and equal to the difference between cell concentrations, divided by the specimen thickness L . Under these conditions, Fick’s law applies. For vessel

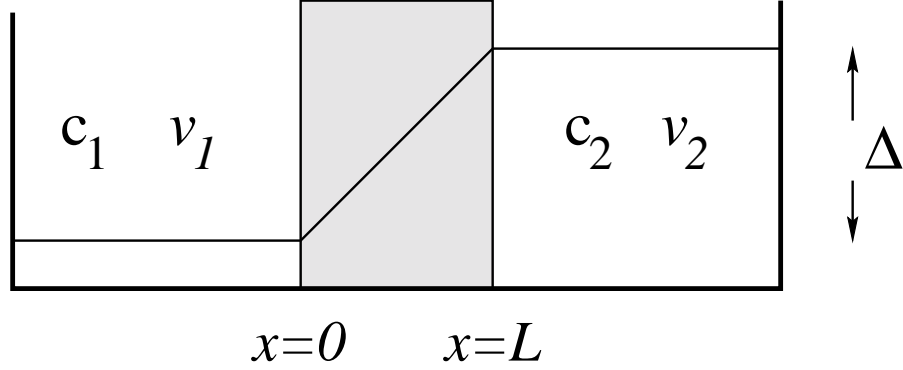


Figure 9: Schematic of the constant gradient hypothesis across a sample with thickness L . Vessels 1 and 2 contain an aqueous electrolyte with target species concentrations c_1 and c_2 , and have volumes v_1 and v_2 , respectively.

volumes v_1 and v_2 and specimen area A , the difference in concentration Δ between the two vessels can be shown to decay exponentially [35, 39]:

$$\frac{\Delta}{\Delta_0} = \exp \left[\frac{-D^a A}{L} (v_1^{-1} + v_2^{-1}) t \right] \quad (35)$$

The quantity Δ_0 is the concentration difference at the onset of a linear concentration profile. Based on Eqn. 35, a semi-log plot of the concentration difference between the two vessels should appear as a straight line under ideal conditions; the magnitude of the slope being proportional to the apparent diffusion coefficient D^a . Deviations from a straight line will indicate behavior that cannot be modeled by Fick's law with a constant apparent diffusion coefficient.

4.2.4 Formation Factor Measurement

The formation factor measurements were performed using KCl as the pore solution because the conductivity of a few standard solutions are known to a high precision [37]. A range of concentrations was used to ensure that the surface conduction component was properly accounted for. For the conductivity measurement, the specimen was vacuum saturated with potassium chloride solution and then mounted, using rubber o-rings and clamps, between two glass vessels, each containing a platinum electrode. The setup is shown schematically in Fig. 10(a). The apparatus, in the absence of a specimen and holder, had a conductivity cell constant of 0.3567 cm^{-1} .

To determine the formation factor of the saturated specimen, the cell was filled with the same solution as the saturation solution and then allowed to thermally equilibrate in the environmental chamber. The direct current (dc) resistance of the specimen and cell was determined using a commercial impedance spectrometer that sampled frequencies between 10 Hz and 1 MHz [22]. The bulk conductivity of the specimen was calculated

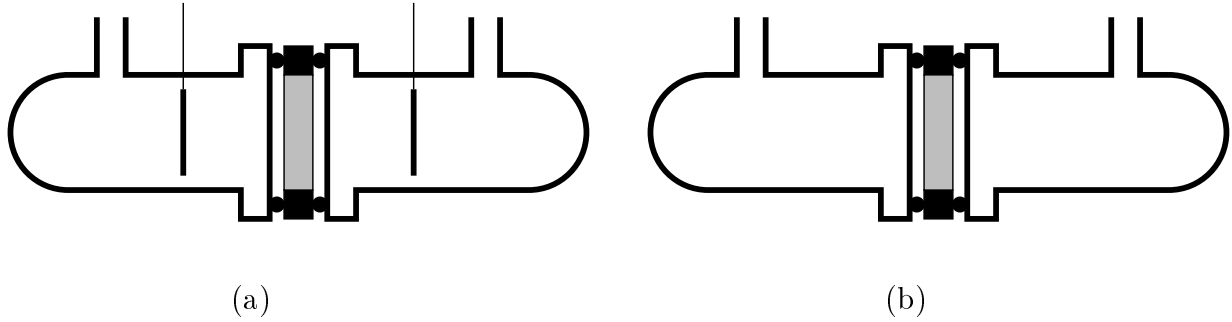


Figure 10: The conductivity cell apparatus(a) and the diffusion divided cell apparatus (b). The schematics depict the configuration of the two cylindrical glass vessels on either side of a mounted specimen. The system is sealed using rubber o-rings; the clamps are not shown. The apparatus differ only in the vertical platinum electrodes in the conductivity cell. The diameter of the specimen, the glass vessels, and the platinum electrodes are approximately 50 mm.

from the cell constant and the specimen geometry. The formation factor was calculated from the ratio of the conductivity of the KCl solution to the calculated bulk conductivity.

Pore solution concentrations of $0.01 \text{ mol}\cdot\text{kg}^{-1}$, $0.10 \text{ mol}\cdot\text{kg}^{-1}$, and $1.00 \text{ mol}\cdot\text{kg}^{-1}$ were used to assess the contribution from surface conduction. Due to a small surface conduction contribution, the formation factor increased with increasing pore solution conductivity, converging to a fixed value with increasing concentration. The specimen conductivity measured using the $0.01 \text{ mol}\cdot\text{kg}^{-1}$ solution was approximately 85 % of the value using the $1.0 \text{ mol}\cdot\text{kg}^{-1}$ solution, and the specimen conductivity using the $0.10 \text{ mol}\cdot\text{kg}^{-1}$ solution was approximately 98 % of the value using the $1.0 \text{ mol}\cdot\text{kg}^{-1}$ solution. Therefore, the formation factor calculated at $1.0 \text{ mol}\cdot\text{kg}^{-1}$ was used as the best estimate. Since the change in formation factor was only 2 % for a ten fold increase in concentration, the true value is probably not more than a fraction of percent larger than the values reported.

Since the ceramic specimens are the result of a controlled commercial process, they have relatively little specimen to specimen variation. The four specimens used in this experiment had formation factors ranging from 10.6 to 10.9. These values were determined after each specimen was allowed sufficient time to reach thermal equilibrium, and then the values of the dc resistance varied by less than 1 %.

4.3 Formation Factor vs. Diffusion Coefficient

Upon completion of the conductivity measurement to determine the formation factor, the specimen was then saturated with KI and placed into a divided cell apparatus shown schematically in Fig. 10(b). The objective was to determine the value for the formation factor F required in Eqn. 32 in order for the calculated iodide concentrations to agree with the experimental values.

The measured values of Δ for the iodide concentration are shown as symbols in Fig. 11. For each of the four systems, the concentration of the KI is equal to the concentrations

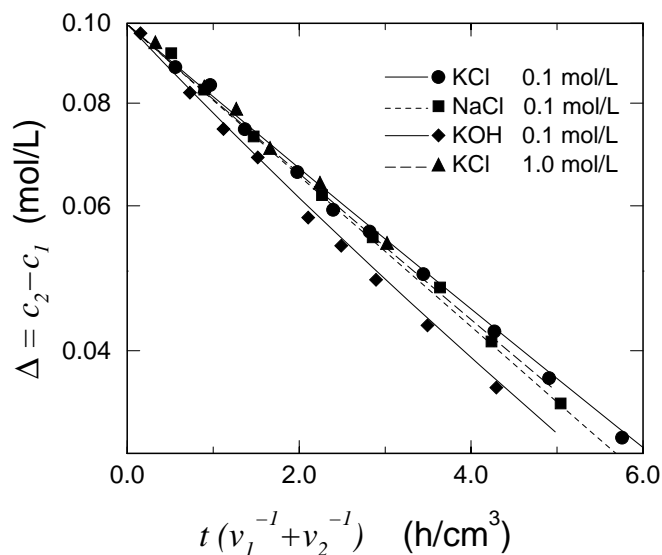


Figure 11: Concentration difference across each specimen as a function of time normalized by the vessel volumes. The experimental values are shown as filled symbols, the estimates by 4SIGHT are shown as solid curves. The measurement uncertainties would appear as the same size as the symbols, so are omitted for visual clarity. The value of Δ for the 1.0 mol/L KCl system is divided by ten in order to appear on the same scale as the other data.

shown in the figure key. The estimated measurement uncertainties are approximately the size of the symbols, and are not shown as error bars for reasons of visual clarity. The KCl and the NaCl systems behaved similarly; the values of Δ for the 1.0 mol/L KCl system were divided by ten so that they could be included on the same plot. The 1.0 mol/L KCl solution has a similar behavior to the 0.1 mol/L KCl system because the self diffusion coefficients D^s for K^+ , Cl^- , and I^- are nearly equal to one another. The estimated diffusion potential ψ_D (Eqn. 32 across the entire specimen for both of the KCl systems) was less than 1 mV, and was less than 5 mV for the NaCl system. The KOH system showed a marked difference in behavior. One reason for this is that the self diffusion coefficient D^s for OH^- is significantly greater than that of the other ions present, resulting in a calculated diffusion potential of approximately 16 mV. A diffusion potential of this magnitude could have a noticeable effect on the transport of the iodide ions.

The calculated slopes of the experimental data from semi-logarithmic plots are shown in Table 4. The estimated standard deviations shown are typically less than 3 % of the slope value, suggesting that the constant gradient assumption is valid for these systems. In fact, the systems reached a constant gradient state at a relatively early age. Analysis using the 4SIGHT computer program suggests that the constant gradient condition is achieved in less than 12 h.

Also shown in Table 4 are the values for the ratio D^s/D_b , using the iodide value for D^s ($2.045 \times 10^{-5} \text{ cm}^2 \text{ s}^{-1}$ [23]). This ratio represents an incorrect use of the formation factor to determine the apparent bulk diffusion coefficient. Since the quantity D^s in this

Table 4: The values for the slope (AD_b/L) of the experimental data shown in Fig. 11. Also shown is the ratio D^s/D_b , using D^s for iodide. The uncertainties shown for the slopes are the estimated standard deviation reported by the statistical software, and also characterize the uncertainty in the ratio D^s/D_b reported.

System	AD_b/L ($\text{cm}^3 \cdot \text{h}^{-1}$)	D^s/D_b
KCl – 0.1 mol/L	0.2004 ± 0.0032	11.1
NaCl – 0.1 mol/L	0.2118 ± 0.0032	10.3
KOH – 0.1 mol/L	0.2381 ± 0.0047	9.3
KCl – 1.0 mol/L	0.2079 ± 0.0050	10.7

ratio is a constant, the ratio is inversely proportional to the apparent bulk diffusivity D_b . This ratio does not reflect the actual formation factor, however, because the iodide self diffusion coefficient within the pore solutions is not equal to D^s . Also, it is clear that future changes in the pore solution will lead to changes in the apparent bulk diffusion coefficient of iodide in these systems, while the formation factor is nearly equal for all systems.

The values of the formation factor F were determined from the experimental data using the 4SIGHT implementation of Eqn. 32, and are shown in Table 5, labelled F_{sim} . Also shown in the table are the values of the formation factor calculated from the impedance spectroscopy measurements, labelled F_{IS} . The uncertainty in F_{IS} reflects the variation in the dc resistance measurement as mentioned previously. To estimate F in Eqn. 32, its value was adjusted until the calculated values of Δ agreed with the measured values; this value is referred to here as F_{sim} . The values of F_{sim} shown in Table 5 were used to calculate values for Δ , and these values of Δ are plotted in Fig. 11, denoted by the lines. The experimental data and the calculated values for the KCl and the NaCl systems were all nearly linear, suggesting that the linear Fick’s law for diffusive transport is valid for these systems. The values of Δ for the KOH system are easily distinguished from the other systems.

The calculated values of F_{sim} shown in Table 5 were consistent with the measured values F_{IS} . The values of F_{sim} varied by approximately 7 %, compared with the 18 % variation in the values of D^s/D_b . The differences between the values of F_{sim} and F_{IS} were less than 3 % for the KCl and the NaCl system, and less than 8 % for the KOH system. The consistent bias of calculated values of F_{sim} being larger than F_{is} may be attributed to the method of using a single measurement for the specimen conductivity, rather than using a more rigorous approach.

Sighting along the KOH data in Fig. 11 reveals noticeable curvature. It is interesting to note that the computed output (solid curve) also exhibits this nonlinear behavior. This suggests that this nonlinear behavior is due to effects of the pore solution chemistry since output from 4SIGHT indicates that the iodide concentration profile across the sample is stable within 12 h. The calculated concentration profile of iodide, however, is not linear

due to the diffusion potential.

Table 5: Measured and calculated formation factors from impedance spectroscopy (F_{IS}), computer simulation (F_{sim}), and apparent diffusivity (D^s/D_b) using D^s for iodide.

System	F_{IS}	F_{sim}	D^s/D_b
KCl – 0.1 mol/L	10.7±0.2	10.9	11.1
NaCl – 0.1 mol/L	10.9±0.2	11.2	10.5
KOH – 0.1 mol/L	10.6±0.2	11.4	9.3
KCl – 1.0 mol/L	10.7±0.2	10.6	10.7

This electro-chemical effect of the KOH system is revealed in Table 5. As shown in Table 4, the apparent diffusion coefficient of iodide in this system is considerably greater than that for the other systems. The computer calculation reveals that the required formation factor F_{sim} is comparable to the values for the other test solutions. This demonstrates the effect of using the apparent diffusion coefficient D_b to characterize a microstructure. For KOH solution, the apparent diffusion coefficient describes how the iodide ion behaves in the presence of KOH, but does not characterize its behavior in the presence of other test solutions. Similarly, it does not necessarily characterize how other ions behave in the same, or similar, microstructure.

Since the pore solution of cementitious systems is typically alkaline, the results for the KOH system have direct relevance to the prediction of ion transport in portland cement systems. The pore solution ionic strength in cementitious systems can be nearly ten times greater than the 0.1 mol/L KOH system studied here. Further, there will be number of additional ions present, with a corresponding number of self diffusion coefficients. This raises the question of the correct method for characterizing the microstructure of these systems. Either estimating the formation factor from diffusion data or estimating the diffusion coefficient from a formation factor measurement (conduction test) will require knowledge of the pore solution chemistry. For a formation factor measurement that uses pore solution extraction, a chemical analysis of the extracted pore fluid would be a logical extension of the measurement procedure. However, diffusion measurements typically do not reveal the chemical makeup of the pore solution, and so further experimentation may be required for experimental programs based upon diffusion measurements to characterize the microstructure of cementitious systems.

4.3.1 Multi-Species

The results for the multi-species experiments are divided between two series. In the first series, the kinds of ionic species present were kept constant but the initial iodide concentration differences were varied. In the second, the initial iodide concentration were held constant, but the kinds of other species present were varied. The first series attempts to demonstrate the effect of concentration. The second attempts to demonstrate the effect of speciation.

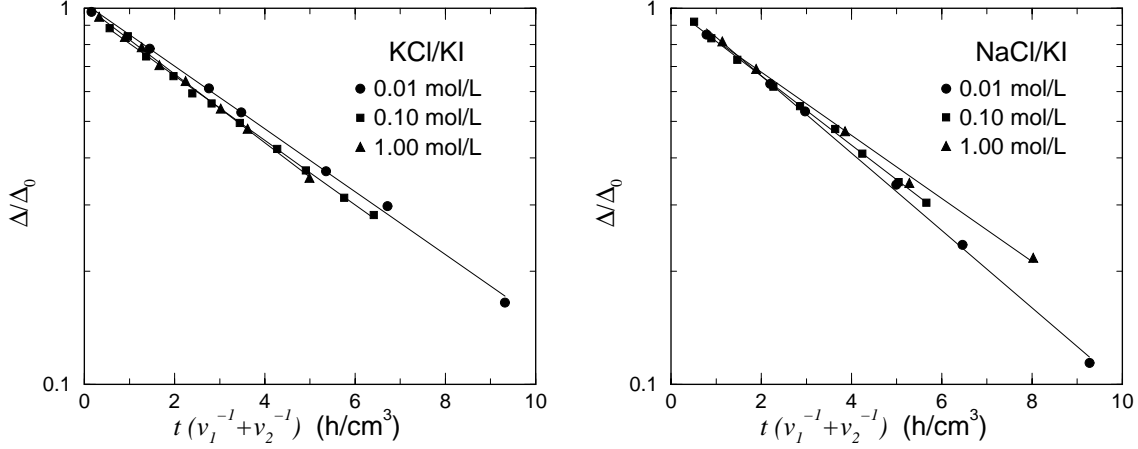


Figure 12: Concentration difference Δ of iodide (filled symbols) for the KCl/KI and the NaCl/KI systems; the time t is scaled by the vessel volumes v_1 and v_2 . The quantity Δ_0 is the initial KI concentration. The lines shown are the result of the linear regression analyses reported in Table 6. The measurement uncertainties are approximately the size of the symbols used.

The experiments with varying concentration were performed with either potassium chloride or sodium chloride as the counter-diffusing electrolyte, with respect to potassium iodide. Plots of the experimental results are shown in Figs. 12. For both the KCl/KI and the NaCl/KI systems, the data exhibit virtually linear behavior on the semi-logarithmic plots. The apparent linear behavior suggests that these systems behave in a nearly “ideal” manner, and can be characterized accurately by Fick’s law in Eqn. 10. Due to the nearly equal self-diffusion coefficients for potassium, chloride, and iodide, there is only a relatively small electrical diffusion potential across the sample.

The magnitude of the slope calculated from the data at each concentration is reported in Table 6. The uncertainties reported are the estimated standard deviations reported by the regression software, and have the corresponding coverage factor [40] $k = 1$. For the three concentrations, the coefficient of variation of the estimated slopes was 5 % for the KCl/KI systems, and 10 % for the NaCl/KI systems. While the differences among slopes, being greater than the estimated uncertainties, suggest that these variations are statistically significant, for practical use, these variations are minor. Any chemical reactions that might occur within the cementitious matrix can alter the diffusion coefficient, easily overwhelming a 20 % uncertainty in the apparent diffusion coefficient.

The experiments with constant KI concentration and varying speciation were performed with KCl, NaCl, KOH, K_2CO_3 , $CaCl_2$, H_2SO_4 , and $MgSO_4$ as the counter-diffusing electrolyte. In all cases, the initial concentration of KI was 0.10 mol/L. The concentration of the counter-diffusion electrolyte was chosen to minimize an osmotic pressure gradient across the sample; it is not asserted here that the values used eliminated an osmotic pressure gradient.

Table 6: Absolute value of the slopes calculated from the data for the KCl/KI and the NaCl/KI systems in Figs. 12, regressed to a linear model. The uncertainties shown are the estimated from standard deviations reported by the regression software, with a corresponding coverage factor of $k = 1$.

Species	concentration (mol/L)	Slope (cm ³ /h)
KCl/KI	0.010/0.010	0.1923±0.0039
	0.100/0.100	0.1978±0.0029
	1.000/1.000	0.2101±0.0024
NaCl/KI	0.010/0.010	0.2365±0.0051
	0.100/0.100	0.2120±0.0024
	1.024/1.000	0.1931±0.0059

The experimental data are shown in Figs. 13, and the analyses of the data are divided between the “short” time and the “long” time results. In Fig. 13(a), a linear model was regressed to the data for which $t(v_1^{-1} + v_2^{-1}) < 8 \text{ h/cm}^3$. The results from the linear regression analyses are shown in Table 7. The uncertainties reported are the estimated standard deviations reported by the regression software, and have the corresponding coverage factor [40] $k = 1$. Based on these results, the CaCl₂/KI system and the K₂CO₃/KI system represent the extrema, and are shown in Fig. 13(b) for all time, along with the KCl/KI system, which is an example of nearly ideal behavior, as a means to contrast the results.

Table 7: Magnitude of the slope for data shown in Fig. 13(a), regressed to Eqn. 35 for $t(v_1^{-1} + v_2^{-1}) < 8 \text{ h/cm}^3$. For each system, the KI concentration was 0.10 mol/L. Also shown are the values for the formation factor F used to produce the solid curves Fig. 13(b). The uncertainties shown are the estimated from standard deviations reported by the regression software, with a corresponding coverage factor of $k = 1$.

Counter Solution	concentration (mol/L)	Slope (cm ³ /h)	F
K ₂ CO ₃	0.0769	0.1581±0.0014	11.7
H ₂ SO ₄	0.0859	0.1688±0.0075	9.6
MgSO ₄	0.1660	0.1867±0.0022	13.5
KCl	0.1000	0.1978±0.0029	11.4
NaCl	0.1000	0.2120±0.0024	11.8
KOH	0.0879	0.2333±0.0034	11.2
CaCl ₂	0.0731	0.2801±0.0089	12.8

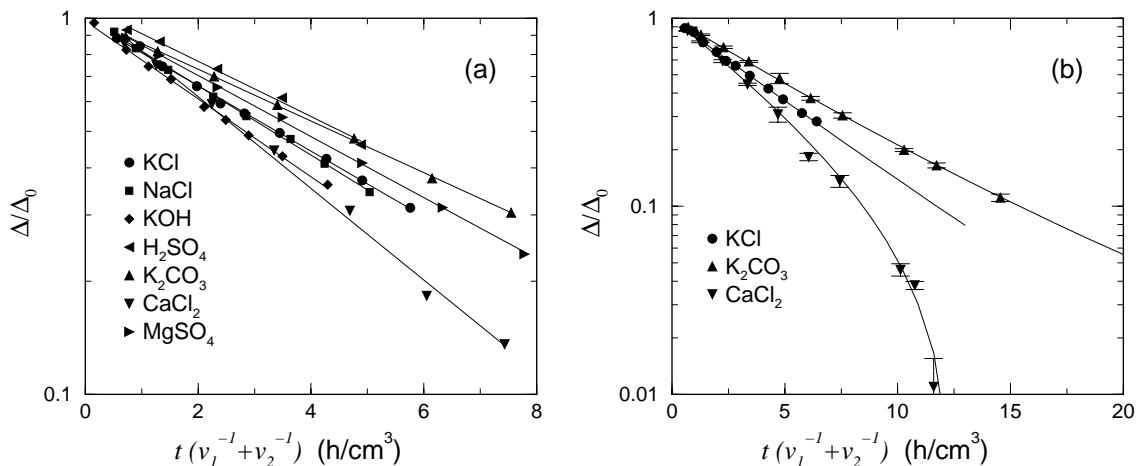


Figure 13: Measured concentration difference Δ of iodide (filled symbols) for constant 0.10 mol/L KI concentration and varying counter-diffusing species; the time t is scaled by the vessel volumes v_1 and v_2 . In (a) results from linear regression (solid lines) for $t(v_1^{-1} + v_2^{-1}) < 8$ h/cm³; the calculated slopes are reported in Table 7. In (b) the electro-diffusion equation is used to estimate the formation factor F , the values of which are shown in Table 7. The error bars represent an estimated standard deviation.

The computed slopes given in Table 7 indicate the effect of speciation on the observed diffusion coefficient. The magnitude of the slopes shown in the table varies by nearly a factor two. This contrasts with the previous 20 % variation in slopes due to concentration.

The CaCl₂ and the K₂CO₃ data are shown in Fig. 13(b) to delineate the envelop over which the concentrations could vary over long times. Note that for long times the slopes of the curves are not constant. While the change in slope for the K₂CO₃/KI system is gradual, the change in slope for the CaCl₂/KI system is dramatic by comparison. Therefore, it is inappropriate to characterizing iodide transport in the CaCl₂/KI system using Fick’s law and a constant apparent diffusion coefficient. Further, the apparent iodide diffusion coefficient decreases slightly in the K₂CO₃/KI system and increases greatly in the CaCl₂/KI system. Any “adjustments” to an apparent diffusion coefficient to account for one system would certainly not apply to another. This is analogous to determining the apparent diffusion coefficient under one set of conditions and using that to extrapolate to behavior in the field with varying species exposure.

By contrast, the data for each system were analyzed using the 4SIGHT implementation of Eqn. 32. The porosity remained fixed at 0.26 and the formation factor remained the only free parameter. The value of the formation factor F required to best approximate the measured data, for all times, is shown in Table 7 for each system. The coefficient of variation for these values was approximately 10 %. The corresponding results are shown as solid curves in Fig. 13(b). The curves for the other systems are not shown for clarity. Further, remaining systems had only minor curvature by comparison.

The important feature of the electro-diffusion equation is that it can capture the

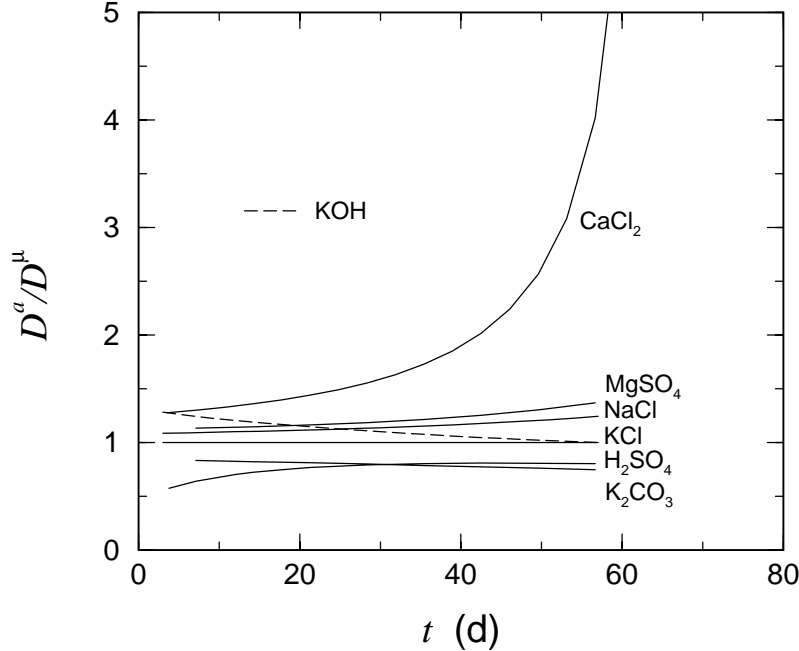


Figure 14: The ratio of the apparent diffusion coefficient D^a to the microstructural diffusion coefficient D^μ (as calculated by 4SIGHT using Eqn. 14) of iodide for the various counter diffusing electrolytes, as a function of time t .

nonideal behavior of these systems. The apparent diffusion coefficient can be calculated at any time from the slope of the curve based on the electro-diffusion equation. This calculated apparent diffusion coefficient can then be compared with the microstructural diffusion coefficient. The results from this comparison are shown in Fig. 14 for all the systems considered in Fig. 14.

The curves shown in Fig. 14 express quantitatively the deficiency in characterizing multi-species diffusion with a single apparent diffusion coefficient. Accurately characterizing the diffusive transport of iodide in these nonreactive systems using Fick's law requires that the apparent diffusion coefficient vary in time. For the CaCl_2/KI system, the apparent diffusion coefficient has increased by a factor of 5 at 60 d.

The surprising result was the behavior of the CaCl_2/KI system at very long time. The curve for the CaCl_2/KI system in Fig. 13(b) appears to be diverging at long times. Analysis of the experimental setup using the electro-diffusion equation predicts that the concentration difference between the vessels will become *negative*; this is equivalent to a *negative* apparent diffusion coefficient as the flux of iodide ions is in the direction of the low concentration to high concentration. The concentration differences Δ for the CaCl_2/KI system are shown in Fig. 15(a) on a linear scale. After approximately 70 d, the experimentally measured concentration difference was, in fact, negative. As a means of comparison, the corresponding data for the $\text{K}_2\text{CO}_3/\text{KI}$ system are shown in Fig. 15(b).

Also shown in Figs. 15(a) and 15(b) are the relative concentration differences for all the species present, as calculated by Eqn. 35. For the CaCl_2/KI system, the “slow” species is the Ca^{2+} ion. For the $\text{K}_2\text{CO}_3/\text{KI}$ system, it is the CO_3^{2-} ion. The effect of these

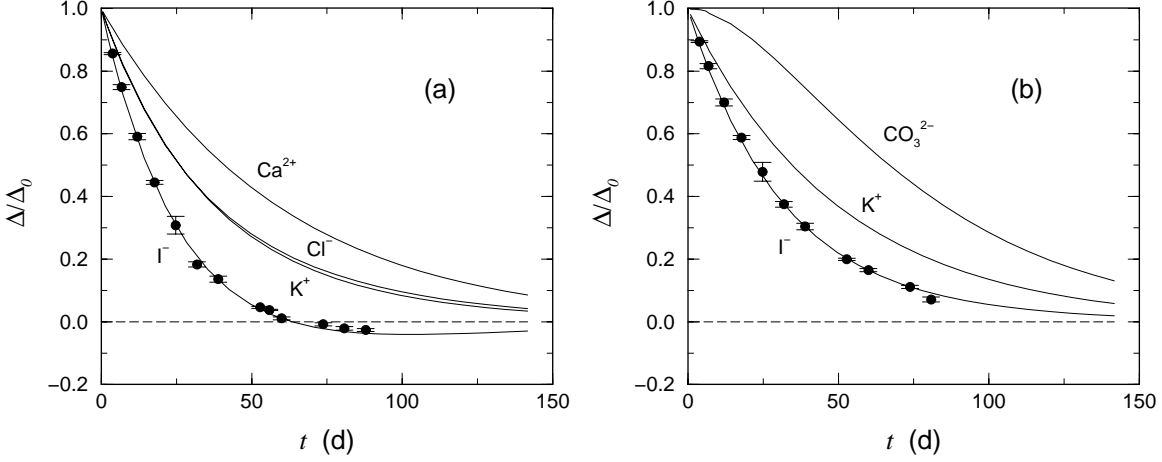


Figure 15: Experimental concentration difference Δ of each diffusing species in the (a) CaCl_2/KI , and the (b) $\text{K}_2\text{CO}_3/\text{KI}$ systems, each as a function of time t . The experimental values are shown as filled symbols, and the curves are the values calculated by 4SIGHT. The error bars represent an estimated standard deviation.

two ions is to greatly control the macroscopic diffusion potential across the specimen. The presence of the Ca^{2+} generates a diffusion potential that is positive with respect to the KI side. Correspondingly, the CO_3^{2-} ion generates a negative potential with respect to the KI side. The result is a macroscopic diffusion potential that accelerates the iodide ion in the CaCl_2 system, and retards it in the K_2CO_3 system. In the CaCl_2 system, the macroscopic diffusion potential is sufficient to drive iodide from the KI vessel to the CaCl_2 vessel, even though the iodide concentration in the KI vessel is less than that of the CaCl_2 vessel. In time, the diffusion potential decreases and the concentration difference Δ approaches zero.

4.4 Summary

Since each of the degradation mechanisms considered by 4SIGHT are controlled by the transport of ionic species throughout the concrete, it is imperative that the transport portion of the 4SIGHT computer program be as accurate as possible. The first step was to validate the transport equation Eqn. 32 used by 4SIGHT. It was shown that the formation factor used in Eqn. 32 is equivalent to the formation factor that can be calculated from conductivity measurements. The second step was to demonstrate that the transport equation characterizes the transport of all the ions present in the electrolyte, and that the only two parameters required are the porosity and formation factor. By characterizing the transport of all the species present, and the resulting macroscopic diffusion potential, the 4SIGHT computer program successfully predicted the occurrence of an experimental setup that could exhibit a negative apparent diffusion coefficient (based on Fick's law). Although only iodide concentration measurements were performed, the wide variation

of behavior of the different experimental setups suggests that the complete system was modeled accurately. Future experiments where all diffusion species concentrations are measured are needed to confirm this.

5 Parameter Uncertainty

As the complexity of service life estimation increases, it is clear that deterministic calculations have diminishing utility. One cannot say with absolute certainty, what the performance of a facility will be over a period of decades or centuries. Rather, one can only offer probabilistic statements of possible outcomes.

To facilitate a probabilistic risk assessment, 4SIGHT allows the user to specify input parameters with both a mean and a level of uncertainty. These uncertainty parameters are then used to generate random deviates based on a random number generator. Multiple service life calculations are performed, each using a new random deviate. The failure times for each calculation is recorded. The results are then reported as a cumulative distribution of failure times.

5.1 Random Deviates

The basis for the random deviate calculation lies in the ability to generate a random deviate from the uniform distribution over the interval (0,1). This is accomplished using a random number generator (see Ch. 7 of Ref. [41]). The resulting uniform random deviate η_i is then used to calculate a random deviate X_i from an arbitrary probability density function $f(x)$:

$$\int_{-\infty}^{X_i} f(x)dx = \eta_i \quad (36)$$

The random number generator used by 4SIGHT is from Knuth [42], and referred to as `ran3` in *Numerical Recipes* [41]. It has been shown that this random number generator is sufficiently robust for calculations involving 10^7 deviates.

5.2 Distributions

Four probability density functions $f(x)$ are provided to the user by 4SIGHT. These four distributions can be used to characterize random deviates over a broad range of uncertainty.

5.2.1 Delta Function

The delta function (see Refs. [43, 44]) is equivalent to having a deterministic value. The delta function is, in a practical sense, a Gaussian distribution with zero variance. The symbol typically used for the delta function is $\delta(x - x_o)$, and a plot of the function would consist of a vertical line at $x = x_o$. A delta function has the following mathematical definitions [44]:

$$\int_{-\infty}^{+\infty} \delta(x) dx = 1$$
$$\int_a^b g(x)\delta(x - x_o) dx = \begin{cases} g(x_o) & a < x_o < b \\ 0 & \text{otherwise} \end{cases} \quad (37)$$

The probability density function $f(x)$ is written mathematically as follows:

$$f(x) = \delta(x - x_o) \quad -\infty \leq x \leq +\infty \quad (38)$$

Every random deviate x_i will have the same value x_o :

$$x_i = x_o$$

5.2.2 Uniform Distribution

The uniform distribution allows one to specify a range over which values can vary; values cannot be used that lie outside the specified width of the distribution. As its name implies, random deviates are chosen uniformly over the specified range, characterized by a center at x_o and a width w . Values are chosen uniformly between $x_o - w/2$ and $x_o + w/2$:

$$f(x) = \frac{1}{w} \quad x_o - \frac{w}{2} \leq x \leq x_o + \frac{w}{2} \quad (39)$$

Using the uniform random deviate η_i over the interval $(0,1)$, the random deviate x_i is calculated from the center x_o and width w of the distribution:

$$x_i = x_o + w \left(\eta_i - \frac{1}{2} \right)$$

5.2.3 Gaussian Distribution

The Gaussian distribution is familiar. For a mean $\mu = x_o$ and variance σ^2 , the probability density function can be stated mathematically as follows:

$$f(x) = \frac{\exp \left[\frac{-1}{2} \left(\frac{x-x_o}{\sigma} \right)^2 \right]}{\sqrt{2\pi}\sigma} \quad (40)$$

Using standard software routines [41], a random deviate ξ_i is calculated from the Gaussian distribution with zero mean and unit standard deviation. The normal random deviate ξ_i can then be used to calculate a random deviate from a Gaussian distribution with mean x_o and variance σ^2 :

$$x_i = x_o + \sigma \xi_i$$

5.2.4 Lognormal Distribution

An advantage of the lognormal distribution is that it can characterize uncertainty over orders of magnitude. Although an entire family of n-th order logarithmic distributions exist [45], the basic feature of a lognormal distribution is that the logarithms of the deviates are normally distributed. This fact can be exploited to simplify deviate generation.

Consider experimentally determined quantities y_i that are the result of a measurement process, and can be characterized by a lognormal distribution (e.g., hydraulic conductivity). Let the variable z_i represent the logarithms (base 10) of these values: $z_i = \log_{10}(y_i)$. Let x_o denote the average of the values of z_i . Let σ represent the standard deviation of

the values z_i . Given an normal random deviate ξ_i with zero mean and unit variance, a logarithmically distributed random deviate x_i can be generated in the following way:

$$x_i = 10^{x_o + \sigma \xi_i} \quad (41)$$

5.3 Output: Cumulative Distribution

For the Monte Carlo calculations, the user will specify a number N of iterations. For each iteration, new random deviates will be calculated and the time at which failure occurs will be calculated; in the absence of failure, the program returns the time limit set by the user. Let each failure time be denoted by t_i , where $1 \leq i \leq N$. The probability density function $g(t)$, giving the probability that the service life of a computational iteration terminated between t and $t + dt$, can be expressed as a sum of delta functions:

$$g(t) = \frac{1}{N} \sum_{i=1}^N \delta(t - t_i) \quad (42)$$

The cumulative probability function $G(t)$ is the integral of the probability density function $g(t)$:

$$\begin{aligned} G(t) &= \int_0^t g(t') dt' \\ &= \frac{1}{N} \sum_{i=1}^N \int_0^t \delta(t' - t_i) dt' \end{aligned} \quad (43)$$

Therefore, under the parameter uncertainty conditions specified by the user, the probability that failure will occur before time τ is simply $G(\tau)$.

This is a mathematically rigorous means of expressing a straightforward concept. An example will clarify the idea further: Consider a service life calculation performed with $N = 10$ iterations, with each iteration using different input parameters, resulting in the following service life termination times:

i	t_i
1	120
2	324
3	80
4	260
5	250
6	210
7	500
8	170
9	500
10	280

The corresponding cumulative distribution function $G(t)$ is given in Fig. 16. These data can then be used within a larger service life calculation composed of a number of elements,

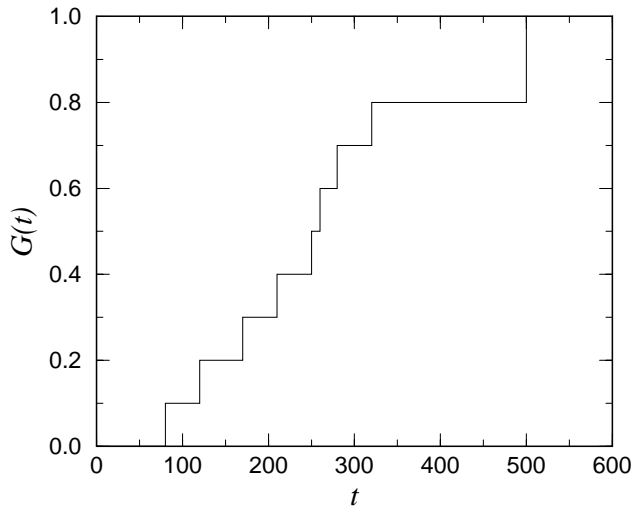


Figure 16: The cumulative distribution function $G(t)$.

of which this is only one. A random failure deviate can be generated from these data by picking a uniform random deviate η_i over the interval $(0,1)$ and solving for t_i from $G(t_i) = \eta_i$.

6 Significance of Cracks

Most degradation processes are due to the presence of some specific ion within the cement paste microstructure. These deleterious ions typically penetrate the microstructure by diffusion and/or advection. To obtain an understanding of the relative magnitude of these mechanisms, consider their contribution to the ionic flux. For diffusivity D , ion concentration c within the capillary pores, and pore solution velocity \mathbf{u}_p , the flux \mathbf{j} is a sum of contributions from diffusion and advection:

$$\begin{aligned}
 \mathbf{j} &= -D\nabla c + c\mathbf{u}_p \\
 &= -D\nabla c + c\frac{\mathbf{v}_D}{\phi} \\
 &= -D\nabla c + c\frac{-k}{\phi\mu}\nabla P
 \end{aligned}
 \tag{44}$$

Here, the permeability k is the bulk permeability that is often reported. The second line in Eqn. 44 represents the pore velocity as a function of the Darcy (bulk) velocity \mathbf{v}_D and capillary porosity ϕ . The third line contains the substitution for the Darcy velocity as a function of the permeability k , pore fluid viscosity μ , and hydraulic pressure P . For a 0.45 water:cement ratio (w/c) concrete, the relevant material parameters can be estimated from the previous 4SIGHT report [1] and are shown in Table 8.

Table 8: Material parameters a concrete with w/c = 0.45, estimated from equations in Ref. [1]. (Default degree of hydration $\alpha = 0.85$)

Parameter	Symbol	Value
diffusivity	D	$7 \times 10^{-12} \text{ m}^2 \text{ s}^{-1}$
permeability	k	$1 \times 10^{-19} \text{ m}^2$
viscosity	μ	10^{-3} Pa s
porosity	ϕ	0.11

The gradients in Eqn. 44 can be estimated from “order of magnitude” values. The length scale is approximately 1 m, the concentrations on the order of 1 mol, and the hydraulic pressure a tenth of an atmosphere (10^4 Pa). The contributions to the flux are 7×10^{-12} for the diffusive transport and 9×10^{-12} for the advective transport. Therefore, this scenario represents an approximate equality between the relative contributions to the overall flux. Changes in either the concentration or the hydraulic gradients would change the contributions, respectively. Since cracks in concrete have permeabilities that are orders of magnitude greater than the permeability of uncracked concrete, their impact on the ionic flux can be dramatic.

6.1 Internal Body Force

The previous report [1] contained a model for advective transport through uncracked concrete that included a term for the body force of ρg (ρ is the fluid density and g is

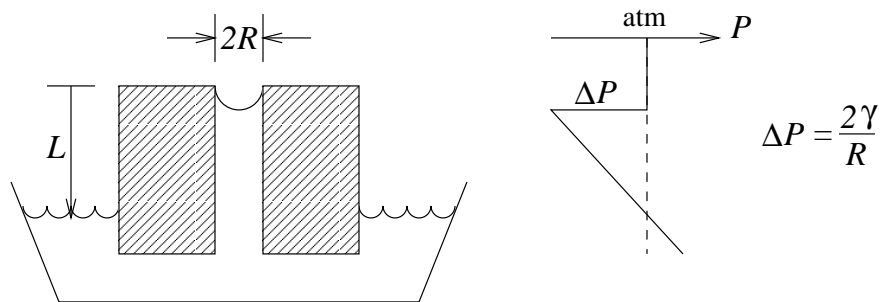


Figure 17: Schematic of water sorption in concrete. The hashed region represents a cross section, with pore radius R and liquid-air surface tension γ , with its bottom surface under water. To the right is a plot of the hydraulic pressure P as one traverses vertically through the pore. Negative pressure indicates water in tension.

the gravitational acceleration), adding a constant to the pressure gradient. This term contributed to the overall advective transport through the concrete. While this addition is accurate for a large saturated specimen with water at both ends, it is not accurate when either end is exposed to an unsaturated environment. Exposure to an unsaturated environment will lead to the formation of menisci in the cement paste pore system. Under many possible conditions, the pressures developed by these menisci are sufficient to prevent the water from “draining” out of the concrete due to gravity.

6.2 Sorptivity

Typical capillary sorptivity tests demonstrate that concrete is not a self-draining material. A dry concrete specimen placed onto a free surface of water will draw the water into the concrete due to capillary sorption. If allowed to contact the water for a sufficiently long period of time, and assuming the height of the concrete specimen is less than 10 m (hydraulic head of one atmosphere), the concrete will, given sufficient time, become saturated with the water.

Concrete is able to retain water because of the menisci formed by a wetting liquid with surface tension γ in pores of radius R . For a concrete of thickness L resting upon a surface of water, the menisci within the pores at the top surface of the concrete specimen generate a pressure drop of $2\gamma/R$ as one passes from the air above into the pore fluid just below the menisci surface. The pressure is sufficient to overcome the head pressure of ρgL , thereby drawing water in from the bottom surface. This condition is shown schematically in Fig. 17. The pores in concrete are sufficiently small that, for concrete in contact with water on its bottom surface and in contact with air at the top surface, the concrete will remain saturated, and there will be no downward flow of pore fluid. This gives an effective hydraulic head pressure of zero. In fact, for an unsaturated environment at the

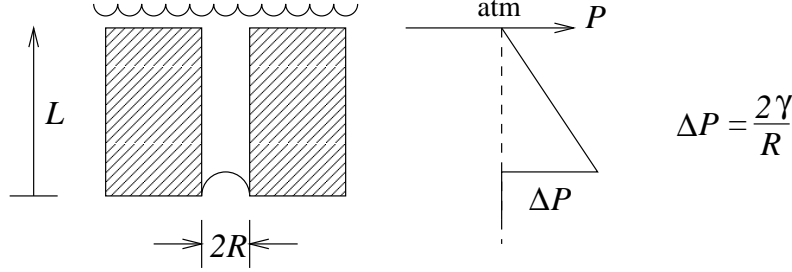


Figure 18: Schematic of the hydraulic pressures in a porous material with a thin layer of water on its top surface and unsaturated air exposure on its bottom surface.

top surface, the water will wick away due to evaporation, creating an *upward* movement of fluid.

6.3 Break-Through Pressure

The effect of the menisci can also be applied to a concrete with water on its top surface and exposed to air at the bottom surface. If the bottom surface of a concrete is exposed to an unsaturated environment, the bottom surface of the concrete will have menisci in the pores, analogous to the previous discussion. Imagine a very shallow pool of water exists on top of a concrete specimen with thickness L . The hydraulic pressure within the concrete increases as $\rho g z$, with z represented the distance below the surface of the water above the concrete. At the menisci on the bottom surface, there is a pressure increase of approximately $2\gamma/R$ as one passes from the pore fluid to the air below the specimen. This is shown schematically in Fig. 18.

The minimum specimen thickness L required for the flow of water through the specimen can be calculated from the balance of these pressures:

$$\rho g L = \frac{2\gamma}{R} \quad (45)$$

In SI units, $\rho = 1000 \text{ kg}\cdot\text{m}^{-3}$, $g = 9.8 \text{ m}\cdot\text{s}^{-2}$, and $\gamma = 0.0735 \text{ N}\cdot\text{m}^{-l}$ (liquid-vapor surface at 15°C). The approximate value for the menisci radii corresponding to a given permeability can be approximated from the Katz-Thompson relationship:

$$k = \frac{F}{200} d_c^2 \quad (46)$$

The quantities k , F , and d_c are the specimen permeability, formation factor, and critical pore diameter, respectively. For typical concretes of good quality, $k = 10^{-17} \text{ m}^2$ and $F = 500$. Using the critical diameter d_c as an estimate of the meniscus diameter, this

approximation gives $R = 1.0$ nm. The corresponding hydraulic head is 15 000 m. This is also an estimate of the hydraulic head required to overcome the effect of surface tension or order for flow to initiate. And since the hydraulic pressure increases as $\rho g z$ both inside concrete and in free water, for a thin film of water over the concrete, the specimen would have to be 15 000 m thick in order for flow to initiate. Although this calculation was a rough approximation, this minimum thickness is nearly four orders of magnitude greater than one would expect for a vault roof. Therefore, one would not expect water to flow through a vault roof that had a thin film of water on its top surface, and an exposure of unsaturated air on the bottom surface.

This simple calculation demonstrates the significant effect that an unsaturated environment at the lower concrete surface can have an advective transport through undamaged concrete. By keeping the interior environment of the vault below saturation, the advective flow through the concrete will be virtually zero.

6.4 Transport Through Cracks

The preceding section demonstrated the significance of having undamaged concrete in contact with a unsaturated interior vault. In practice, the concrete will likely have some distress that will cause cracking, and may have a far different performance than undamaged concrete.

One can characterize the effects of cracks by calculating the minimum crack width before water will flow through the concrete. Consider a horizontal concrete slab that is 1 m thick. Assume that the slab is saturated, that there is a shallow film of water on the top surface, and that the bottom surface is exposed to an unsaturated environment like that shown in Fig. 18. The $\rho g h$ hydraulic pressure is just able to “push” water through a 15 μm crack (assuming plane, parallel walls) which would cause dripping from, or pooling on, the bottom surface of the concrete. A 15 μm crack is generally invisible to the naked eye, yet its effect upon the advective transport through the concrete is dramatic. Clearly, to accurately quantify advective transport through concrete one has to accurately quantify the cracking within the concrete.

6.4.1 Residence Time

Using this more clearly constructed description of the effects of cracks, it should be much easier to characterize flow through the cracks, and to estimate a residence time for the time required for water to traverse the concrete member. If there exist cracks either at the bottom of the slab or through the entire slab, there should be mass flow, even if the atmosphere of the vault is unsaturated with respect to water vapor. Knowledge of the residence time is needed in order to characterize the chemistry of the effluent into the interior of the vault. If the residence time is sufficiently short, the fluid will not have sufficient time to reach equilibrium before passing through the concrete. This effect directly effects any attempt to predict the chemistry of the effluent from the vault.

The residence time for a crack can be calculated using Darcy’s law. Within a vertical crack, there is a body force of ρg downward on the water. This corresponds to a constant

pressure gradient: $\nabla P = -\rho g$. Darcy's law gives the bulk fluid velocity \mathbf{v}_b :

$$\mathbf{v}_b = -\frac{k}{\mu} \nabla P \quad (47)$$

The averaged pore velocity \mathbf{v}_p , is greater than the bulk velocity by a factor of the porosity:

$$\mathbf{v}_p = \frac{\mathbf{v}_b}{\phi} \quad (48)$$

Therefore, the residence time t_r for a fluid to pass through a sample of thickness L is $t_r = L/\mathbf{v}_p$. For a quality concrete ($k = 10^{-18} \text{ m}^2$) 1 m in thickness, with 1 m of head, the Darcy velocity is less than $1 \text{ }\mu\text{m/d}$. The corresponding residence time is 2 700 years.

For cracked concrete, the Darcy velocity is much greater. As an example, consider a 1 m thick slab with a $100 \text{ }\mu\text{m}$ crack extending through the entire slab. Since the permeability of plane, parallel surfaces separated by a distance w is $w^2/12$ [47], the permeability of the $100 \text{ }\mu\text{m}$ crack is $8.3 \times 10^{-10} \text{ m}^2$. Assuming the pore fluid density and viscosity are approximately equal to those of water, for an equivalent water head of 1 m, the bulk velocity \mathbf{v}_b through the crack is 8.3 mm/s . For the $100 \text{ }\mu\text{m}$ crack, $\mathbf{v}_p = \mathbf{v}_b$, and the residence time t_r is approximately 120 s. Therefore, the issue of pore fluid residence time in cracked concrete is important.

6.4.2 Evaporative Mass Transfer

In cases where a concrete is kept saturated and there are cracks at on the interior surface, water will probably advance to the surface of the concrete where these cracks exist. Given the size of typical cracks, the equilibrium relative humidity of an atmosphere exposed will be nearly 100 % RH. Therefore, a vault interior environment below saturation will cause evaporation of the concrete pore fluid that is in the cracks.

Assuming that the concrete permeability of the uncracked portion is sufficiently great so as to supply these cracks with additional pore solution, there should be a thin film of water on the interior surface of the concrete. The rate of evaporation from the bottom surface can be approximated from formulas for evaporation from a free surface of water. The saturation pressure P_S (Pa) of water can be expressed as a function of its temperature T (in Celsius) [46]:

$$P_S(T) = 610 \exp \left[\frac{17.3 T}{237.3 + T} \right] \quad (49)$$

Let $P_S^c(T_c)$ and $P_S^a(T_a)$ represent the saturation pressure of water at the temperature of the concrete (T_c) and of the air (T_a), respectively. Exposed to an atmosphere with relative humidity ξ and with wind speed (forced convection, if applicable) v_w , (m s^{-1}) across the concrete surface, the water evaporation rate E ($\text{kg}\cdot\text{m}^{-2}\cdot\text{s}^{-1}$) is [46]

$$E = (8.69 \times 10^{-5}) (P_S^c - \xi P_S^a)(0.253 + 0.017 v_w) \quad (50)$$

For an underground concrete structure, the temperature of the concrete would be equal to the vault temperature. Therefore, the evaporation rate equation for a concrete vault at temperature T simplifies slightly:

$$E(T) = (8.69 \times 10^{-5}) P_S(T) (1 - \xi) (0.253 + 0.017 v_w) \quad (51)$$

This is the most general result. If the interior atmosphere of the vault is maintained constant through convection, the wind speed will be non-zero. If the vault interior is sealed, the evaporation rate will reach zero over time.

Once the evaporation rate is determined, it can be compared with the advective flux. If the evaporation rate is less than the advective flux, there will exist accumulations of pore solution on the bottom surface of the roof, and this accumulation will drip onto the contents of the vault.

7 Predicting Drying Shrinkage and Flexural Cracks

A recent review of the 4SIGHT computer model [47] revealed that the most important factor affecting ionic transport through concrete is the presence of cracks. The presence of cracks not only controls the quantity of ions transported, but can also control whether there will be convective transport in the absence of externally applied hydraulic pressure. That recent review is reproduced here nearly in its entirety for completeness.

Cracking can originate from within the concrete due to a number of mechanisms. During the placement of the concrete, if the evaporation rate is great enough, the concrete surface can develop tensile stresses sufficient to crack the plastic concrete. These *plastic shrinkage cracks* typically extend through the section of the concrete. If during placement the concrete member experiences settlement, and the concrete has insufficient strength to withstand the resulting stresses, the concrete will undergo *settlement cracking*. If the concrete member is a slab that spans a distance, the concrete surface in tension (typically the bottom surface) will possibly develop *flexural cracks* after removal of the concrete form work. During the cement paste hydration, a large portion of the initial mix water will be consumed, with the generation of heat. Differences between concrete temperature and ambient temperature can lead to *thermal cracking*, depending on the mechanical state of the concrete. The continued removal of water by the hydration process will generate a chemical shrinkage stress that can initiate *autogeneous shrinkage cracks*. Subsequent drying due to ambient conditions will also generate a shrinkage strain that can initiate *drying shrinkage cracks* when the concrete is restrained.

Some cracks are to be expected, while others are the result of improper construction practices. Plastic shrinkage cracking, thermal cracking, and settlement cracking can be either avoided or minimized by following industry guidelines (ACI Manual of Concrete Practice) for the placement and curing of concrete. Both flexural cracks and shrinkage cracks are to be expected (under the assumptions given above), and the resulting crack widths and spacings can be estimated. Therefore, the incorporation of crack modeling by 4SIGHT will be limited to the prediction of flexural and shrinkage cracking and their effect on transport.

The models for the crack width and spacing described here will be implemented into a structural analysis of a vault that is meant to represent a typical design. Under ideal conditions, a structural engineer would perform an analysis of the specific vault in question, and then input the calculated parameters into 4SIGHT. The structural analysis presented is not meant to represent an exhaustive analysis. It is the default analysis, however, that will be performed in the absence of any analysis by the engineer who is using 4SIGHT.

To proceed, one must assume an approximate geometry for a representative vault structure. The principles used here for estimating the composite permeability due to cracking are general enough to apply to many different vault designs. A general geometry and construction plan for the vault will be assumed here to illustrate the analysis.

To partially simplify the structural analysis, the vault will be approximated by a container with horizontal dimensions L_1 and L_2 such that their ratio is greater than two: $L_1/L_2 > 2$. The corresponding edge loads f_1 and f_2 have a quartic dependence on

length [48]:

$$\frac{f_1}{f_2} = \frac{L_2^4}{L_1^4} \quad (52)$$

Since the load carried in the direction of the shorter span is 16 times greater, the vault analysis will be performed using one-way slab behavior.

The spacing and width of both shrinkage and flexural cracks depends strongly on the amount and the location of the steel reinforcement. In addition, the positive moment due to the load will depend on how the roof is attached to the vault walls. The roof could either rest on the walls (simply supported) or it could be rigidly attached to the walls (continuous reinforcement). For a given geometry and load, the simply supported roof will be subjected to approximately twice the positive moment of a fixed end roof.

Although an analysis that assumes a simply supported roof would result in a greater estimated positive moment, it is quite unlikely that simply supported construction would occur in practice. By definition, a simply supported roof must be able to rotate and translate freely over the vault walls. While this type of construction can eliminate drying shrinkage cracks, the joint provides a likely path for the ingress of fluids and ionic species.

In addition to the analysis of the flexural and shrinkage crack formation at the center of the roof, there will exist negative moments at the connection between the roof and the walls. Although an analysis of negative moment cracks is not performed here, the method for incorporating these cracked sections into the overall composite properties follows from the positive moment analysis. In addition, no analysis of the shear stress at the joint between the roof and the wall is presented.

The scenario adopted here is that the vault will first be filled with waste materials, compacted, and the roof cast in place on top of the vault contents. The expected thickness of the vault roof is assumed to be 1 m, and the contents of the vault will probably settle under the dead load of the roof and the soil above the vault. The roof will then flex, possibly forming flexural cracks. In fact, a small amount of flexure will be useful in that it will help close shrinkage cracks at the top surface.

7.1 Cracked Reinforced Concrete

Given the construction plan outlined above, the concrete roof will likely experience shrinkage stresses during the first months, and later experience flexural stresses as the vault contents settle over time. While the flexural stresses will widen the shrinkage cracks on the bottom of the roof, they will contract the shrinkage cracks on the top surface of the vault. The reinforced concrete containing both shrinkage and flexural cracks will have a permeability that is greater than the uncracked concrete.

7.1.1 Crack Model

For simplicity, the cracks are approximated by plane parallel walls separated by the observed crack width. The open cracks on the tension face of the roof propagate upwards to the neutral axis. While the depth of crack penetration is accurate, the approximation of the cracks by plane parallel walls is conservative. This assumption does not account

for either the “V” shape of the crack or the crack wall surface roughness, both of which would act to reduce the crack permeability with respect to one with plane parallel sides.

The permeability k' of a crack with plane parallel sides is solely a function of the crack width w [47]:

$$k' = \frac{w^2}{12} \quad (53)$$

7.1.2 Composite Permeability

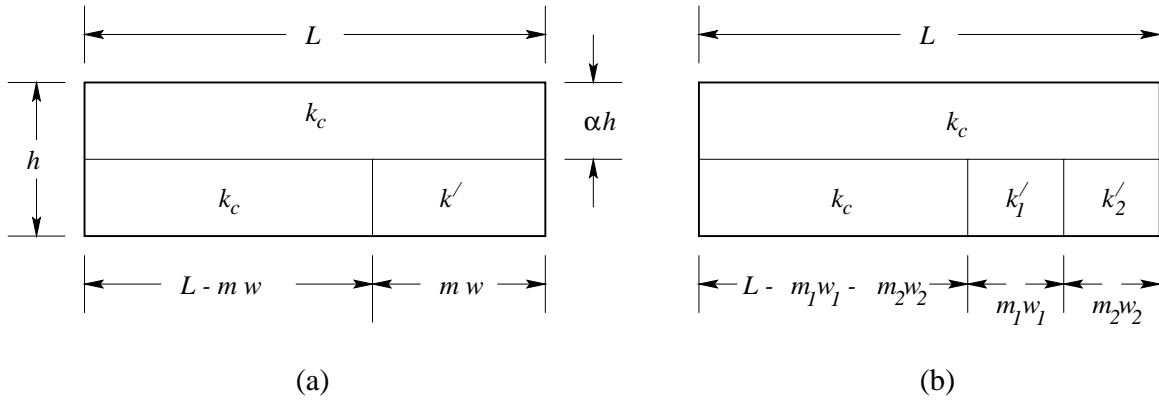


Figure 19: Composite models for the bulk permeability of the roof incorporating the uncracked permeability k_c , crack permeability k' , and having a number m cracks over the slab length L : (a) slabs with m cracks, each with width w ; (b) slabs with m_1 and m_2 cracks of width w_1 and w_2 , respectively.

Composite models for the roof bulk permeability are shown in Fig. 19. The cracks propagate from the bottom of the slab up to the neutral axis. The thickness of the slab is h , and the depth to the neutral axis is expressed as the product αh . The permeability of the uncracked concrete is k_c . The composite has an additional component with permeability k' due to m cracks, each with width w , over the entire span L . For Fig. 19(a), the permeability k_b of the two bottom sections k_c and k' in parallel is a weighted average:

$$k_b = \frac{1}{L} [(L - mw) k_c + mwk'] \quad (54)$$

The composite permeability k^* of k_b and k_c (top section in Fig. 19(a)) in series is treated like the corresponding problem of conductors in series:

$$\begin{aligned} \frac{1}{k^*} &= \frac{\alpha}{k_c} + \frac{1 - \alpha}{k_b} \\ k^* &= \frac{k_c k_b}{(1 - \alpha)k_c + \alpha k_b} \end{aligned} \quad (55)$$

Given that a crack with a width of one micrometer has a permeability of $8 \times 10^{-14} \text{ m}^2$, and that concrete permeability is on the order of 10^{-18} m^2 , the second term in Eqn. 56 can be neglected:

$$k^*(k_b \gg k_c) = \frac{k_c}{\alpha} \quad (56)$$

Therefore, for a given concrete mixture, the control of roof permeability is the control of the neutral axis depth, given that there is sufficient flexural strain to close shrinkage cracks at the top surface of the roof.

The relationship between composite permeability and the neutral axis depth should not be used as a means to reduce vault permeability. Within practical limits, the depth of the neutral axis can only affect the composite permeability by a factor of two or three. However, variations in concrete mixture proportions and cementitious materials can change the concrete permeability by a factor of 10 to 100. Therefore, efforts to reduce overall permeability should concentrate on controlling the concrete mixture.

7.1.3 Composite Permeability Model

The way in which the effects of shrinkage and flexural cracks are combined depends upon the formation and the geometry of the cracks. The shrinkage cracks will likely form first, and there will be a number m_s of these cracks, each with width w_s , separated by a distance L_s . Similarly for the flexural cracks, formed independently of the shrinkage cracks, there will be m_f flexural cracks, each with width w_f , separated by a distance L_f . The objective is to consider the formation of the cracks independently, and then determine the properties of the cracked material.

The resulting width and separation of cracks depends on the cracking scenario. Here, the assumption is that the shrinkage cracks form first and the flexural cracks form after the vault contents settle. For the case when the crack spacings are approximately equal, so that $L_s \approx L_f$, the later flexural cracks should simply widen the existing shrinkage cracks. If $L_s \ll L_f$, the flexure should once again widen the existing shrinkage cracks. For the third case when $L_s \gg L_f$, new flexural cracks should form in between the existing shrinkage cracks, each with width w_f and separated by L_f . If one assumes that the existing shrinkage cracks contribute to the flexural cracking, the shrinkage cracks should also widen by an amount equal to w_f .

The particular crack model to choose from in Fig. 19 depends upon the ratio L_s/L_f . For the first two scenarios presented ($L_s/L_f \approx 1, L_s/L_f \ll 1$), the flexural stress widens the existing shrinkage cracks. Each crack will then have the same width and spacing, corresponding to the model shown in Fig. 19(a). For the third case ($L_s/L_f \gg 1$), there will exist two crack widths and spacings. The existing shrinkage cracks will widen by an amount w_f , and the $m_f - m_s$ flexural cracks will each have a width w_f , corresponding to the model shown in Fig. 19(b). The analysis of this ternary composite bulk permeability k^* follows from the binary example given previously. The parameters for each model are shown in Table 9.

Table 9: Parameters for the composite permeability calculation for m cracks of width w . The crack model refers to that shown in either Fig. 19(a) or Fig. 19(b).

L_s/L_f	Model	w_1	m_1	w_2	m_2
< 1	(a)	$w_s + \frac{m_f}{m_s}w_f$	m_s		
≈ 1	(a)	$w_s + w_f$	m_s		
> 1	(b)	$w_s + w_f$	m_s	w_f	$m_f - m_s$

7.2 Flexural Crack Model

The model for estimating flexural crack widths and spacings is based upon the recommendations given in ACI 224.2R-90 [3]. The recommendation for estimating flexural crack width w_f is the Gergely-Lutz equation:

$$w_f = 2.2 \beta \epsilon_r (d_c A_n)^{1/3} \quad (57)$$

The definitions of the parameters are as follows:

- d_1 : distance from the neutral axis to the tension face
- d_2 : distance from the neutral axis to the centroid of the tension steel reinforcement
- β : the ratio d_1/d_2
- ϵ_r : strain in the tension steel reinforcement
- d_c : minimum concrete cover thickness, measured to center of tension reinforcement
- A_n : the largest area of concrete, perpendicular to the reinforcement, symmetric about the centroid of the tension reinforcement, divided by the number of bars

The estimate of the spacing between flexural cracks is based upon the CEB/FIP model. The maximum distance l_s over which slip can occur can be approximated from the following equation:

$$l_s = \frac{d_r}{3.6 p_s} \quad (58)$$

The quantity d_r is the steel reinforcement diameter, and p_s is the area of steel divided by the effective area of concrete in tension. The average spacing between flexural cracks L_f is taken to be 2/3 this value:

$$L_f = \frac{d_r}{5.4 p_s} \quad (59)$$

7.3 Shrinkage Crack Model

The drying shrinkage model is based upon the calculations of Base and Murray [49] for calculating the width w_s and spacing L_s of shrinkage cracks. The model assumes the member is restrained at its ends and requires the following design parameters:

L : length of slab
 E_s : Young's modulus of the steel reinforcement
 E_c : Young's modulus of the concrete
 n : modulus ratio = E_s/E_c
 A_s : total area of steel in cross section
 A_c : total area of concrete in cross section
 b : slab width
 d : depth of reinforcement
 ρ : reinforcement ratio = A_s/bd
 d_r : steel reinforcement bar diameter
 ϵ_{sh} : shrinkage strain
 ϵ_t : concrete tensile strain at crack initiation

The “no-bond” or slip length a of reinforcement near a shrinkage crack can be approximated from the reinforcement diameter d_r and the reinforcement ratio p :

$$a = 0.08 \frac{d_r}{p} \quad (60)$$

The number of shrinkage cracks m_s that form along a restrained slab of length L can be estimated from the following equation:

$$m_s = 1 + \frac{Lnp}{2a} \left[\frac{\epsilon_{sh} - \epsilon_t}{3 \epsilon_t} \right] \quad (61)$$

The spacing between shrinkage cracks L_s can be estimated from the number of shrinkage cracks m_s over the slab span L :

$$L_s = \frac{L}{m_s + 1} \quad (62)$$

The estimate for the number of shrinkage cracks m_s can be used to estimate the steel stress f_s :

$$f_s = E_s \left(\frac{\epsilon_{sh} + 2\epsilon_t}{3} \right) \left(\frac{L - 2ma}{npL + 2ma} \right) \quad (63)$$

The average shrinkage crack width w_s can be estimated from the following equation:

$$w_s = 2a \left(\frac{f_s}{E_s} + \frac{\epsilon_{sh}}{3} \right) \quad (64)$$

7.4 Design Example

The following is an example of how one can perform a calculation to estimate the spacing, width, and depth of shrinkage and flexural cracks. The calculation begins with the concrete mixture design, estimates the extent of cracking, and then estimates of the composite permeability.

7.4.1 Mixture Design

The mixture design chosen for this example represents a balance between quality of concrete and ease of formulation and placement. The design compressive strength f'_c is 35 MPa, which is within the normal strength guidelines of ACI 211.

The constituent material properties are as follows:

Cement Type	Type I
Cement Density	3.2 g/cm ³
CA Density	2.8 g/cm ³
FA Density	2.6 g/cm ³
Max. Agg. Diameter	25 mm

For a reinforced foundation with a design strength of 35 MPa, the ACI 211 procedure results in the following trial mixture proportion:

Constituent	Mass (kg/m ³)
Water	190
Cement	399
Coarse Agg.	1104
Fine Agg.	757

A high range water reducer is not specified, simplifying the formulation.

Although this mixture is only a trial proportion, it will be used as the final mixture proportion for the purposes of demonstration.

7.4.2 Concrete Properties

Based on the ACI 211 procedure, the concrete is assumed to have the following properties:

w/c	0.43
Slump	75 mm
Air Content	1.5 %
Concrete Density	2450 kg/m ³

In practice, these properties would be determined from tests performed on trial batches and not based on the ACI 211 procedure. As a demonstration, however, the ACI values will be used here.

The equation for estimating the elastic modulus of concrete is described in Nilson [48]:

$$E_c = \left(3320 [\text{MPa}^{1/2}] \sqrt{f'_c} + 6890 [\text{MPa}] \right) \left(\frac{\rho_c}{2330 [\text{kg/m}^3]} \right)^{1.5} \quad (65)$$

This equations can be applied to normal density concretes over a wide range of design strengths: $21 \text{ MPa} \leq f'_c \leq 83 \text{ MPa}$. For the mixture given above, the estimated elastic modulus is 28.6 GPa.

A concrete member in tension will experience a tensile stress f_t . In flexure, the member will remain uncracked until the tensile stresses exceed the modulus of rupture. The estimation for the modulus of rupture f_r is taken from Nilson [48]:

$$0.67 [\text{MPa}^{1/2}] \sqrt{f'_c} \leq f_r \leq 1.0 [\text{MPa}^{1/2}] \sqrt{f'_c}$$

For the mixture used in this example, it is expected that the modulus of rupture f_r can be characterized by the following inequality:

$$4.0 \text{ MPa} \leq f_r \leq 5.9 \text{ MPa}$$

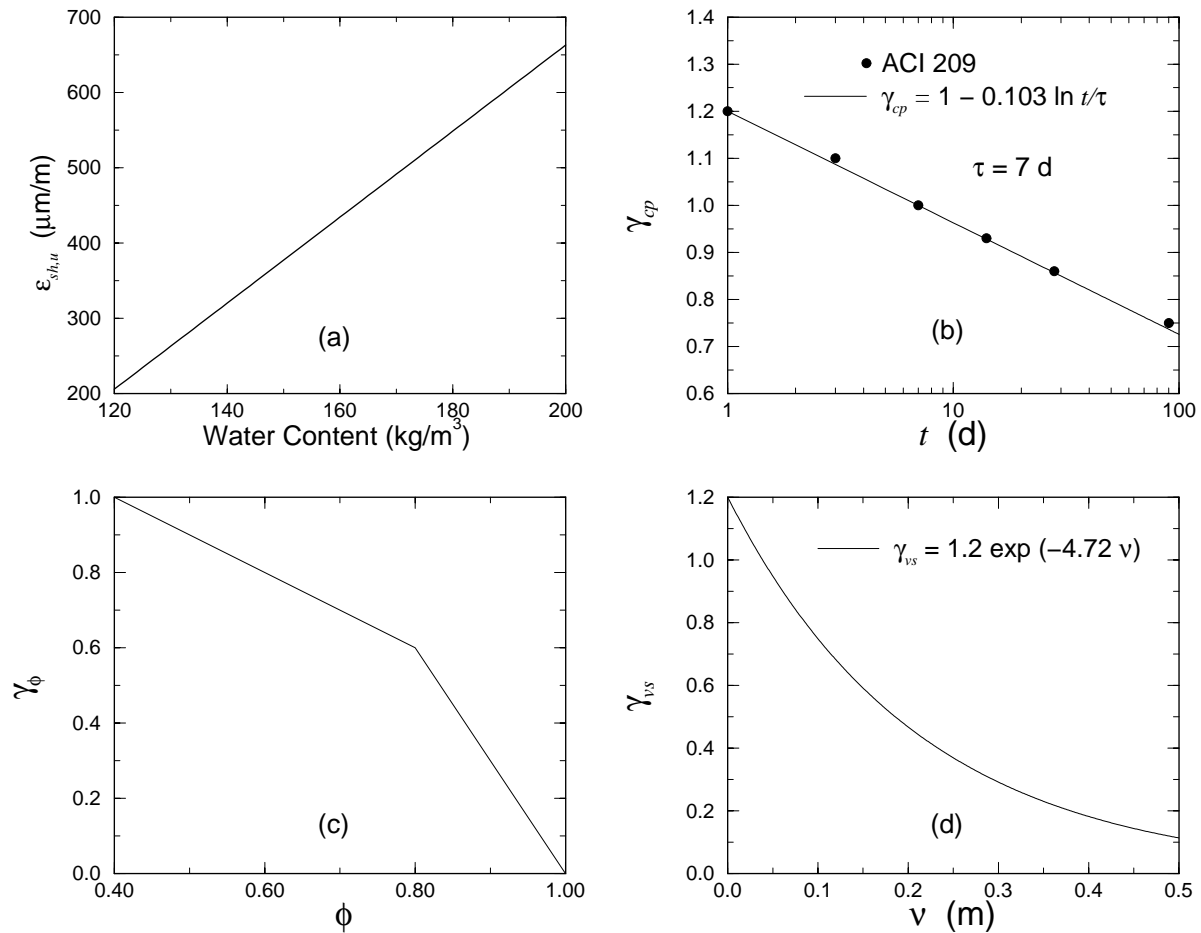


Figure 20: Quantities for estimating shrinkage strain: (a) ultimate drying shrinkage strain under standard conditions; (b) factor γ_{cp} for duration of moist curing; (c) factor γ_{ϕ} for ambient relative humidity; and (d) factor γ_{vs} for the volume to surface ratio.

The ACI guideline for estimating the ultimate drying shrinkage strain $\epsilon_{sh,u}$ is shown in Fig. 20(a) as a function of the mixture water content. For this mixture, the expected ultimate drying shrinkage is approximately 600 $\mu\text{m/m}$.

The expected shrinkage strain ϵ_{sh} will be less than the ultimate value due to mitigating factors. ACI 209R-82 gives the following mathematical expression for the combined effects of these factors on the expected ultimate shrinkage strain:

$$\epsilon_{sh} = \epsilon_{sh,u} \prod_i \gamma_i \quad (66)$$

The quantity $\epsilon_{sh,u}$ is the ultimate shrinkage strain under standard conditions: curing duration of 7 d, exposure to 40 % relative humidity, and a volume-to-surface ratio of 0.038 m.

There are three factors γ_i considered here: duration of curing γ_{cp} ; ambient relative humidity γ_ϕ ; and volume-to-surface ratio γ_{vs} . There are other factors outlined in ACI 209, but the factors relating to concrete mixture design do not apply here since we are using the ultimate drying shrinkage prediction shown in Fig. 20(a).

The factor γ_{cp} for the duration of moist curing is shown in Fig. 20(b) as a function of curing time t . The filled circles are the recommendations from ACI 209, and the curve is an approximation:

$$\gamma_{cp} = 1 - 0.103 \ln \left(\frac{t}{\tau} \right) \quad (67)$$

The value of τ is 7 d, corresponding to the standard curing condition for the duration of moist curing.

The factor γ_ϕ for the ambient environment is shown in Fig. 20(c) as a function relative humidity ϕ . Over the range of relative humidity shown in Fig. 20(c), the factor has two linear regions:

$$\gamma_\phi = \begin{cases} 1.4 - 1.0 \phi & 0.40 \leq \phi \leq 0.80 \\ 3.0 - 3.0 \phi & 0.80 \leq \phi \leq 1.00 \end{cases} \quad (68)$$

It is difficult to estimate the ambient relative humidity for a buried vault. However, most certainly the relative humidity will be greater than 40 % and less than 100 %. As a conservative estimate, the factor γ_ϕ will be assigned a value of one here. However, in practice, an assessment should use a value commensurate with the specific soil conditions being considered.

The factor γ_{vs} for the geometry of the structural element is shown in Fig. 20(d) as a function of the volume-to-surface ratio ν . ACI 209 expresses this factor in analytic form:

$$\gamma_{vs} = 1.2 \exp(-\nu/\nu_o) \quad (69)$$

The quantity ν_o equals 0.212 m, and simply renormalizes ν . For the present design, the length and width of the slab are L and $2L$, respectively. For a slab thickness h , the volume-to-surface ratio ν is the following:

$$\nu = \frac{h}{2 + 3\frac{h}{L}} \quad (70)$$

For a slab thickness h equal to 1 m, and a slab length L equal to 10 m, the volume-to-surface ratio ν equals 0.435 m, corresponding to a shrinkage factor γ_{vs} of 0.15.

The expected ultimate shrinkage strain ϵ_{sh} is the product of the ultimate shrinkage strain under standard conditions $\epsilon_{sh,u}$ and the factors γ_i :

$$\begin{aligned}\epsilon_{sh} &= \epsilon_{sh,u} \gamma_{cp} \gamma_{\phi} \gamma_{vs} \\ &= 90 \mu\text{m/m}\end{aligned}\tag{71}$$

This is significantly less than the 600 $\mu\text{m/m}$ that was based on standard conditions.

7.4.3 Steel Properties

The steel considered for this example is ASTM A 615 Grade 60 steel; a steel with a 60 000 psi yield strength. The corresponding properties in SI units are as follows:

$$\begin{aligned}E_s &= 200 \text{ GPa} \\ f_y &= 414 \text{ MPa}\end{aligned}\tag{72}$$

Therefore, the modulus ratio n , defined as E_s/E_c , is approximately 7.

7.4.4 Reinforcement Ratio Requirements

One of the most important parameters in estimating the bulk permeability of the reinforced concrete element is the depth of the neutral axis. This quantity is estimated from a structural analysis of the complete concrete structure. Ideally, an engineer using 4SIGHT will have access to a structural analysis that includes an estimate of the depth of the neutral axis. In the absence of this information, 4SIGHT must make a reasonable approximation.

The following section is not meant as a primer on structural analysis. Rather, it outlines the procedure 4SIGHT will use to estimate the neutral axis in the absence of such data. If the engineer using 4SIGHT determines that the analysis invoked by 4SIGHT is insufficient, the engineer must then perform a more thorough analysis independently, and report the neutral axis as input to the 4SIGHT computer program.

There is a limit on both the minimum and maximum amount of steel reinforcement allowed in the design of a flexural member. The minimum limit is based on the ability of the element to carry the intended load. The maximum limit is determined by the ultimate failure mode within the reinforced concrete element.

The two regions of stress within the slab are the tension zone in the bottom and the compression zone in the top. At the ultimate load, either the steel will fail in tension, or the concrete will fail in compression. Steel failure in tension is a gradual process, giving “warning” of impending failure. Compressive failure of concrete, by contrast, is a sudden mode of failure. Therefore, there is a maximum limit on the amount of steel reinforcement so as to ensure that the steel will yield before the concrete fails in compression.

The amount of steel at which the two modes of failure coincide at ultimate load is the balanced reinforcement ratio ρ_b :

$$\rho_b = \frac{f'_c}{f_y} \frac{0.85\beta}{1 + \frac{f_y}{600 [\text{MPa}]}} = 0.033\tag{73}$$

For a 35 MPa concrete mixture, the recommended value of β is approximately 0.775.

The maximum allowable reinforcement ratio ρ_{max} is 3/4 of the balance reinforcement ratio:

$$\begin{aligned}\rho_{max} &= 0.75 \rho_b \\ &= 0.025\end{aligned}\tag{74}$$

The minimum reinforcement ratio ρ_{min} can be calculated based on the assumption that a steel stress f_s that is 2/3 of the yield stress is an acceptable limit of steel stress immediately after cracking. The corresponding reinforcement is the following:

$$\begin{aligned}\rho_{min} &= \frac{0.220 [\text{MPa}^{1/2}] \sqrt{f'_c}}{f_y} \\ &= 0.0031\end{aligned}\tag{75}$$

This is in agreement with the ACI 318 recommendation:

$$\begin{aligned}\rho_{min} &= \frac{1.38 [\text{MPa}]}{f_y} \\ &= 0.0033\end{aligned}\tag{76}$$

7.4.5 Roof Geometry

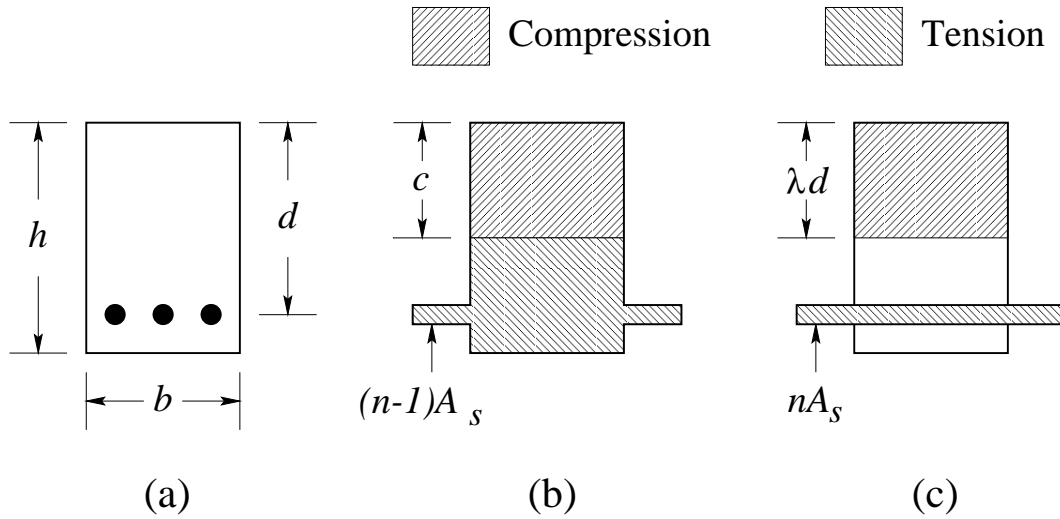


Figure 21: Roof geometry used for analysis: (a) cross section showing location of steel reinforcement (filled circles); (b) transformed section used for uncracked analysis; (c) transformed section used for cracked analysis.

The dimensions of the roof slab are defined in Fig. 21 and are given the following values:

$$\begin{aligned}
h &: 1.0 \text{ m} \\
d &: 0.9 \text{ m} \\
b &: 1.0 \text{ m} \\
d_r &: 35.8 \text{ mm}
\end{aligned}$$

The slab width b is set to 1.0 m to simplify the analysis by normalizing values on a “per meter” basis. The reinforcement diameter d_r of 35.8 mm corresponds to a No. 36 metric bar size or a No. 11 bar in customary inch-pound units.

7.4.6 Positive Moment

The positive moment at the center of the roof slab is determined from the dead load due to the concrete mass and the mass of soil above the vault. The thickness h of the concrete roof is 1 m, and the assumed thickness of soil h_s over the roof is 10 m. The density of the concrete ξ_c is 2450 kg/m³, and the density of the soil ξ_s is assumed to be 1500 kg/m³ (this soil density value is used for demonstration purposes and is not meant to be an accurate estimate of any particular type of soil). The nominal uniform load (pressure) w_n on the roof depends upon the thickness of each element:

$$\begin{aligned}
w_n &= \xi_c g h + \xi_s g h_s \\
&= 171,000 \text{ N/m}^2
\end{aligned} \tag{77}$$

The quantity g is the gravitational acceleration (9.8 m/s²). The design load w_u :

$$\begin{aligned}
w_u &= 1.4 w_n \\
&= 239,000 \text{ N/m}^2
\end{aligned} \tag{78}$$

The quantity 1.4 is the load factor for dead loads.

The positive moment M_+ at mid-span due to the ultimate load w_u is the integral of the load over half the span:

$$\begin{aligned}
M_+ &= \theta \int_0^b \int_0^{L/2} l w_u \, dl \, db \\
&= \theta b \frac{w_u L^2}{8}
\end{aligned} \tag{79}$$

The quantity θ is a factor that depends on the end conditions of the slab. For a simply supported one-way slab, $\theta = 1$. Here, it will be assumed that the slab edge condition corresponds to the end slab of a multi-span roof; one end is restrained and the other is simply supported. Under these conditions, $\theta = 4/7$:

$$M_+ = 1,707,000 \text{ N}\cdot\text{m}$$

7.4.7 Uncracked Analysis

The starting point for the structural analysis is an analysis of the roof assuming that there are neither flexural nor shrinkage cracks. The maximum flexural stress from the design

loads can then be compared to the modulus of rupture. If the flexural stress exceeds the modulus of rupture, the analysis must be repeated assuming flexural cracking.

As the slab flexes, the top portion of the roof will be in compression, and the bottom portion in tension. There will exist a 2-D surface through the midsection of the slab that defines where the concrete is neither in tension nor in compression. This surface is referred to as the neutral axis.

For a member in pure bending (no shearing force) the strains are linearly proportional to the distance from the neutral axis. Since the coefficient of proportionality is same for both the tensile and the compressive strains (within the elastic limit), the location of the neutral axis can be determined by balancing the area moments of the slab cross section.

To simplify the calculation of the tensile and compressive area moments, the reinforced concrete slab cross section is first transformed into an equivalent concrete cross section. Specifically, the steel is replaced mathematically by an area of concrete equal to $(n-1)A_s$, and located at the depth of the reinforcement. This is shown schematically in Fig. 21(b) for this analysis.

The equation for calculating the area moment is the integral of the moment arm r (absolute distance from the neutral axis) over the slab cross section ($da = dr db$):

$$M = \int r da \quad (80)$$

The moment of the area above the neutral axis, which is located at depth c from the top of the slab, is set equal to the moment of the area below the neutral axis:

$$\frac{bc^2}{2} = \frac{b(h-c)^2}{2} + (d-c)(n-1)A_s \quad (81)$$

The quadratic terms in c cancel, yielding an algebraic solution:

$$c = \frac{bh^2 + 2(n-1)A_s d}{2bh + 2(n-1)A_s} \quad (82)$$

The steel area can be expressed as a function of the steel reinforcement ratio ρ :

$$\rho = \frac{A_s}{bd} \quad (83)$$

This can be used to simplify the equation for the neutral axis depth c :

$$c = \frac{d}{2} \left[\frac{\left(\frac{h}{d}\right)^2 + 2(n-1)\rho}{h/d + (n-1)\rho} \right] \quad (84)$$

The neutral axis depth c , as a function of the reinforcement ratio ρ , is shown in Fig. 22. For the uncracked analysis, the depth of the neutral axis is insensitive to the reinforcement ratio.

The stresses within the transformed concrete section will depend upon the moment of inertia I of the transformed slab. The moment of inertia about the neutral axis is the integral of the square of the moment arm over the slab cross section:

$$I = \int r^2 da \quad (85)$$

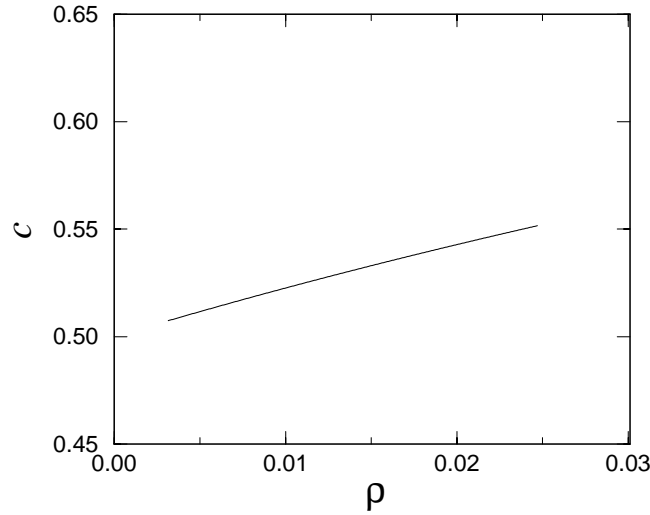


Figure 22: Depth of neutral axis c as a function of the reinforcement ratio ρ for the uncracked analysis.

For the transformed section, the moment of inertia is

$$I = \frac{by^3}{3} + \frac{b(h-y)^3}{3} + (d-y)^2(n-1)A_s \quad (86)$$

For linear elastic behavior, the compressive stress f_c and the tensile stress f_t at the top and bottom surfaces are proportional to the distances from the neutral axis:

$$f_c = M_+ \frac{y}{I} \quad f_t = M_+ \frac{h-y}{I} \quad (87)$$

These quantities are shown in Fig. 23 as a function of the reinforcement ratio p . The compressive stress f_c is approximately one-quarter the design strength f'_c for all values of the reinforcement ratio. By contrast, the tensile stress f_t is considerably greater than the estimated modulus of rupture range of 4 MPa to 6 MPa. Therefore, one expects that the roof slab would develop cracks in the middle portion of the slab.

7.4.8 Cracked Section Analysis

Based upon the previous analysis, it is likely that the concrete roof slab will crack due to flexural loading. These cracks will initiate at the tension surface and continue upward to approximately the neutral axis. Analysis based upon this idea requires a different transformed cross section. This transformed cross section is similar to that of the uncracked transformed cross section except that the concrete below the neutral axis is disregarded.

Determination of the neutral axis for the cracked cross section is similar to the uncracked case. The difference being that one assumes that the concrete in tension does

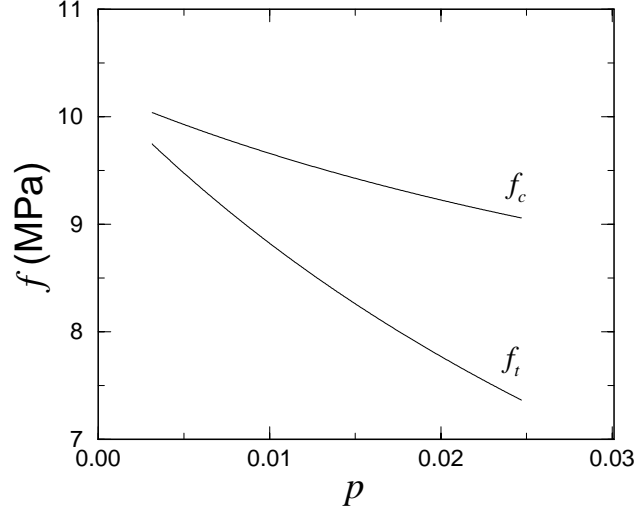


Figure 23: Compressive stress f_c and tensile stress f_t as a function of the reinforcement ratio ρ , based on the uncracked analysis.

not contribute to the moment calculation. This cracked transformed section is shown schematically in Fig. 21(c). The portion of the concrete below the neutral axis is disregarded, and the steel is transformed into an equivalent area nA_s of concrete.

Let the depth of the neutral axis be a fraction λ of the reinforcement depth d . The balance of the area moments about the neutral axis leads to the following algebraic equation:

$$b \frac{(\lambda d)^2}{2} = nA_s(d - \lambda d) \quad (88)$$

The solution for λ is found from the quadratic equation:

$$\lambda = \sqrt{(np)^2 + 2np} - np \quad (89)$$

The neutral axis depth factor λ is shown in Fig. 24(a) as a function of the reinforcement ratio ρ . In contrast to the uncracked section analysis, the depth of the neutral axis for the cracked cross section has a strong dependence on the reinforcement ratio.

The stresses at the compression surface and the steel reinforcement are calculated in much the same way as for the uncracked analysis. The calculation of the cracked section moment of inertia I_{cr} omits the second term on the right hand side of Eqn. 86 because this concrete is in tension. Assuming linear elastic behavior, the compressive stress f_c in concrete at the top surface and the tensile stress f_t in the steel are proportional to their distance from the neutral axis:

$$f_c = M_+ \frac{d\lambda}{I_{cr}} \quad f_t = M_+ \frac{d(1 - \lambda)}{I_{cr}} \quad (90)$$

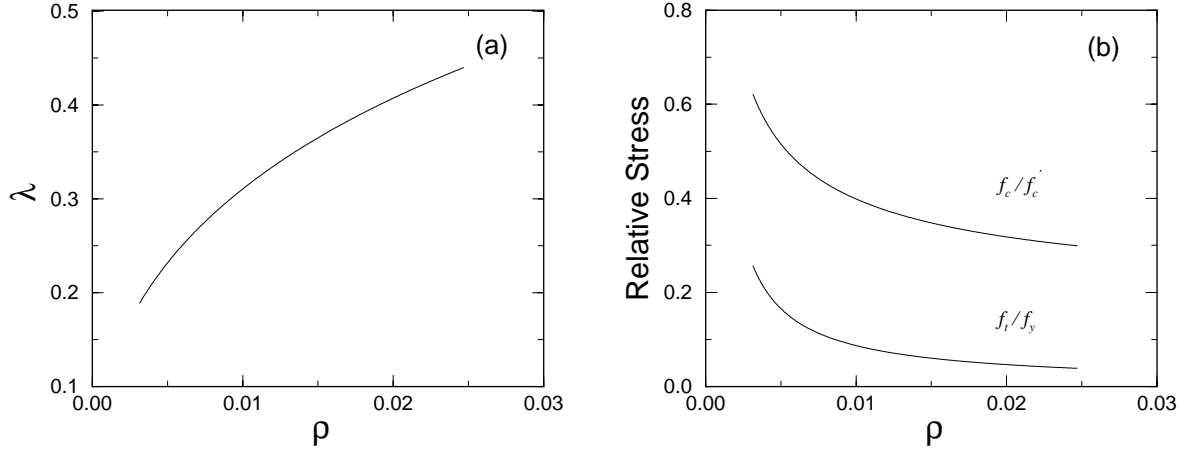


Figure 24: Cracked transformed section analysis: (a) relative depth of neutral axis λ ; (b) relative tensile stress f_t/f_y and compressive stress f_c/f'_c for the cracked section analysis, assuming linear elastic behavior.

The compressive stress f_c and the tensile stress f_t are shown in Fig. 24(b) as a function of the reinforcement ratio ρ . Further, both stresses are normalized by their limiting values. The ultimate compressive stress is f'_c , and the limiting tensile stress is the steel yield stress f_y .

Based on the assumptions that the vault contents will subside and that the roof slab will be a span in flexure, the top surface of the slab should remain in flexure, regardless of the shrinkage strain. The effect of the shrinkage strain, if any, will be to increase the bending moment of the slab. Regardless, the top surface of a linear elastic member in flexure should be in compression, with no open cracks. Therefore, the importance of the structural analysis is to determine the depth of the neutral axis and the width of the cracks within the bottom surface of the slab.

Proceeding further with the analysis requires employing a specific model for combined cracking under flexural and shrinkage stresses. First, one considers the development of the cracks to be independent of one another. Based on this estimation, an estimate of the distances between the final cracks will be formulated based on physical intuition.

An estimate for the final crack width and spacing within the bottom surface of the slab depends on the relative size of the shrinkage and flexural cracks. The estimate for the ratio of shrinkage crack spacing L_s to the flexural crack spacing L_f is shown in Fig. 25(a) as a function of the reinforcement ratio p . Over most of the allowable range for p , the ratio L_s/L_f is greater than five. Therefore, the flexural cracks should develop between shrinkage cracks.

An independent analysis of the shrinkage crack width w_s and flexural crack width w_f are shown in Fig. 25(b) as a function of the reinforcement ratio ρ . From an assessment of the estimate of crack widths, the combined crack widths will certainly be tens, if not hundreds, of micrometers wide. The cracks will occur at the tension face and extend at

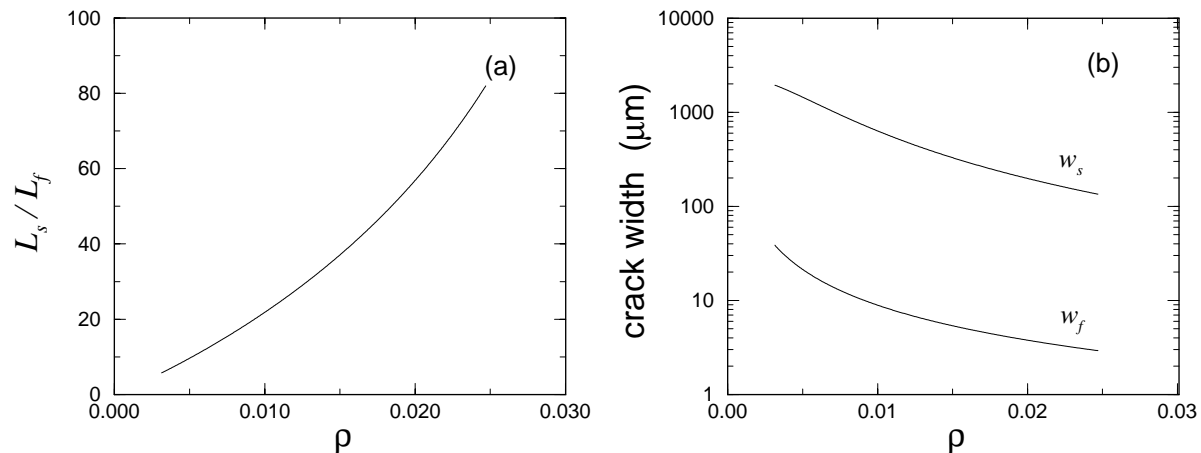


Figure 25: Results of the cracking model: (a) The ratio of the shrinkage crack spacing L_s and the flexural crack spacing L_f ; (b) Flexural crack width w_f and shrinkage crack width w_s .

least to the neutral axis.

7.4.9 Simplified Composite Permeability

Since the permeability of the cracked portion of the slab will be orders of magnitude greater than the uncracked portion of the concrete, further analysis can be simplified by approximating the composite permeability k^* using Eqn. 56:

$$\frac{k^*}{k_c} \approx \alpha^{-1} = \frac{h}{\lambda d}$$

This result is plotted in Fig. 26(a) as a function of the reinforcement ratio ρ . The ratio of the permeabilities increases by less than a factor of five over most of the allowable range of ρ .

Since the exact crack width at the bottom surface of the concrete may become inconsequential, the significance of the structural analysis will be to formulate an accurate estimate for the depth of the neutral axis. This fact is emphasized in Fig. 26(b) that shows a plot of the ratio k^*/k_c as a function of the relative depth to the neutral axis α , for three values of the ratio k_b/k_c . Note that the ratio k^*/k_c converges rapidly with respect to the ratio k_b/k_c . In practice, the ratio k_b/k_c could be orders of magnitude greater than those shown in the graph.

7.5 Probabilistic Approach

A deterministic calculation, like that performed in the previous section, is useful for estimating the probable behavior of the reinforced concrete structure. In practice, however,

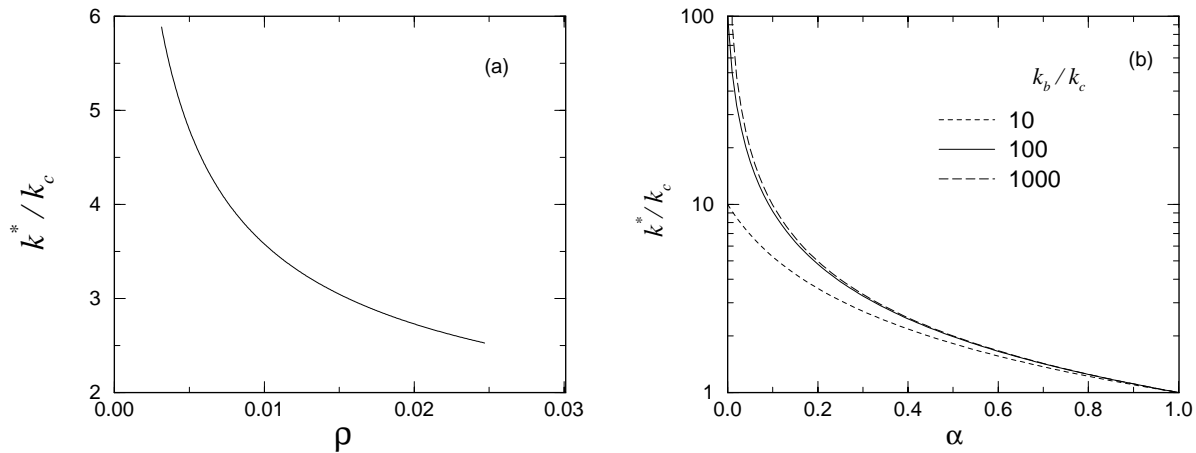


Figure 26: Ratio of the composite permeability k^* to the uncracked concrete permeability k_c : (a) as a function of reinforcement ratio ρ , and (b) as a function of the relative depth to the neutral axis α .

the exact size of the cracks that form will vary, as will the depth of the neutral axis. The resulting variations in these quantities lead to variations in the expected permeability of the structure. In order to capture this variation a probabilistic approach is used.

The probabilistic method employed here is based on a Monte Carlo calculation using parameter uncertainty as a means of characterizing random deviates. Each parameter required for a deterministic calculation has associated with it an estimated uncertainty. With this uncertainty, one can use a computer to repeat the deterministic calculation numerous times, with each iteration using a new random deviate for each parameter. From the multiple calculations, the estimated composite permeability from the each iteration form a population of permeability values, from which a population mean and standard deviation can be calculated. These values can then be incorporated into the service life calculation, which will, in turn, yield an estimated mean and standard deviation for the service life of the structure.

7.5.1 Initial Material Parameters

The following probabilistic analysis follows identically from the previous section with the only exception being that some of the input parameters are normally distributed about some mean value with a coefficient of variation (CoV) (the ratio of the mean to the standard deviation). The parameters allowed to vary are shown in Table 10. Note that the mean values are identical to those used in the previous deterministic analysis. The values for the (CoV) are not meant to be accurate for any particular structure, and are only given for demonstration of the technique. The reader is referred to the ACI 117 report on construction tolerances for general guidance.

The values for the coefficient of variation given in Table 10 are not based on any

Table 10: The mean and associated coefficient of variation (CoV) for the input parameters that would be used in an uncertainty analysis of flexural and shrinkage cracking.

Variable	Property	Mean	CoV
L	Slab length (m)	10.0	0.05
E_c	Concrete Modulus (GPa)	28.6	0.05
f'_c	Concrete compressive strength (MPa)	35.0	0.05
h	Slab thickness (m)	1.00	0.10
d	Depth of steel (m)	0.90	0.05
ϵ_s	Shrinkage strain ($\mu\text{m}/\text{m}$)	90	0.25

particular data. An analysis of particular vault should be done with careful consideration of the construction plans and the project description. For example, the CoV for the slab thickness given above is large compared with normal slab on grade construction. The reason for this is the assumption that the contents of the vault would be compacted remotely, and so the variability of the slab thickness would be greater than for normal practices. Construction plans for specific vaults may vary and warrant a smaller CoV.

For the probabilistic analysis, the randomization is done as a function of the designed reinforcement ratio ρ . For each value of ρ , random values are drawn for the parameters shown above. Using these, the analysis proceeds as for the deterministic analysis. The approach used by 4SIGHT would be to establish a fixed reinforcement ratio ρ and then repeat the analysis at a constant value of ρ , randomizing the input parameters listed above. 4SIGHT would then report the mean and standard deviation of the results at a given reinforcement ratio.

7.5.2 Results

The material and structural parameters given in Table 10 are used to recalculate the same quantities as were calculated for the deterministic analysis. The only difference is that the calculation is repeated many times. Each time, a value for the reinforcement ratio ρ is chosen and then the computer generates a random number for each parameter listed in Table 10. These “randomized” values are then used in the deterministic analysis. The variation in the result indicates the output sensitivity to that parameter, at that value of CoV. Each figure of the results to be shown includes a solid curve indicating the values from the previous deterministic calculations.

The results for the depth of the neutral axis and the relative stresses are shown in Fig. 27 and can be compared directly to Fig. 24. In general, the probabilistic data follow the same trends as in the deterministic case. The calculated depths of the neutral axis shown in Fig. 27(a) are a function of the reinforcement ratio ρ . The results indicate that the uncertainty in the depth of the neutral axis is relatively insensitive to the uncertainty in the input parameters.

By comparison, the relative compressive and tensile stresses shown in Fig. 27(b) are much more sensitive. The variability in the compressive stress ratio f_c/f'_c is dramatic,

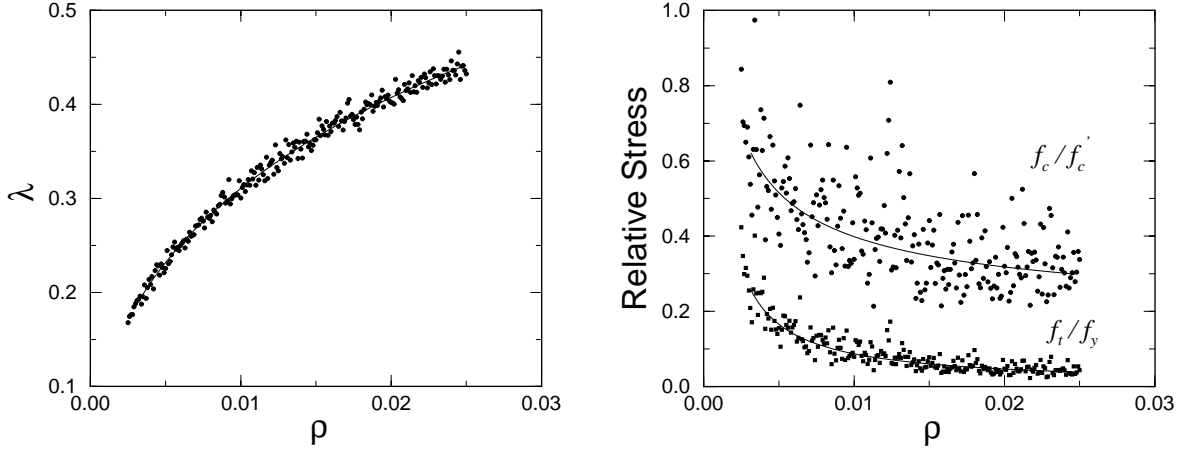


Figure 27: Probabilistic analysis results: (a) Relative depth of neutral axis λ ; (b) Relative tensile stress f_t/f_y and compressive stress f_c/f'_c for the cracked section analysis.

with some of the values approaching one, even for relatively large reinforcement ratios. Since the analysis has been done assuming a linear elastic material, a relative stress greater than 0.5 is probably unreliable. Regardless, the tensile stresses in the bottom of the slab will control the crack width.

The ratio of the shrinkage crack spacing L_s to the flexural crack spacing L_f is shown in Fig. 28(a) as a function of the reinforcement ratio ρ . Although the ratio has large variation, the value is typically far greater than one. Therefore, regardless of the variation in input parameters, one expects that flexural cracks will be initiated between the existing shrinkage cracks.

The shrinkage crack width w_s and flexural crack width w_f are shown in Fig. 28(b). The shrinkage crack widths seem to be insensitive to the variations in the input parameters. Although the flexural cracks appear to be more sensitive, the data are plotted on a logarithmic ordinate which enhances the appearance of variability in smaller quantities.

Since the expected crack widths are still on the order of tens or hundreds of micrometers, the estimate of the bulk concrete permeability k^* can again be simplified with the following approximation:

$$\frac{k^*}{k_c} \approx \frac{h}{\lambda d}$$

This result is shown in Fig. 29. Since the depth of the neutral axis was fairly insensitive to the variability of the input parameters, the relative bulk permeability is also relatively insensitive to parameter variation. The added variation over λ is due to the variability in the roof thickness h and the depth of steel reinforcement d .

The result shown in Fig. 29 is significant because it reveals that the details of the drying shrinkage model are relatively unimportant. Rather, the most significant factors in predicting the permeability of a reinforced concrete structure is the permeability of the sound concrete, and the depth of the neutral axis. Therefore, the two most important

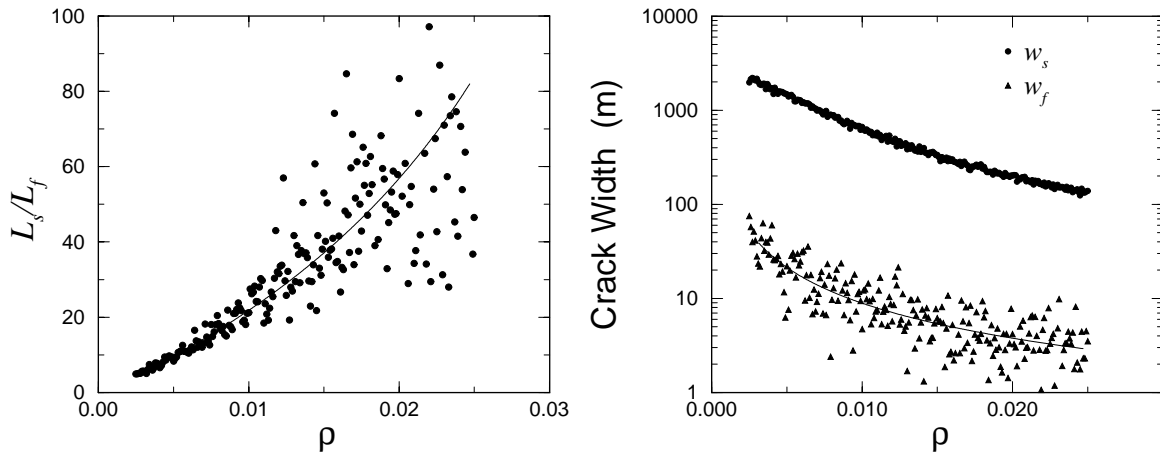


Figure 28: Results of the probabilistic analysis of the cracking models: (a) the ratio of the shrinkage crack spacing L_s to the flexural crack spacing L_f ; (b) flexural crack width w_f and shrinkage crack width w_s .

requirements of the engineering using 4SIGHT to assess a concrete vault is an accurate estimation of the sound concrete permeability and an accurate estimate of the depth of the neutral axis.

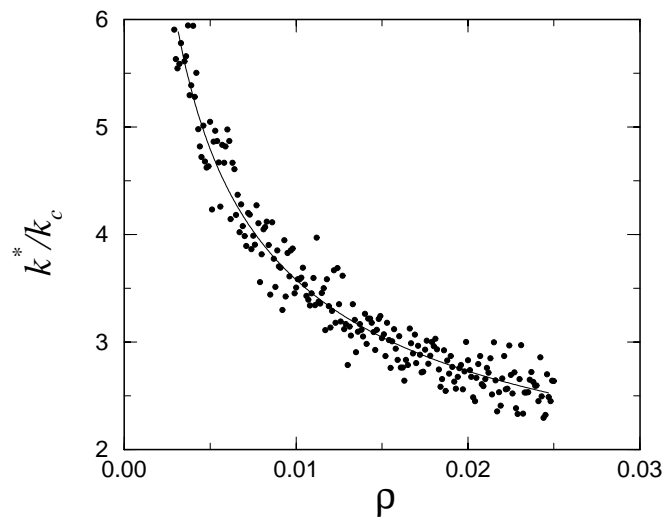


Figure 29: From the probabilistic analysis, the ratio of the composite permeability k^* to the uncracked concrete permeability k_c .

8 User's Guide

An evaluation of the previous user interface to 4SIGHT revealed unnecessary complexity. In an effort to simplify the use of 4SIGHT, a number of assumptions have been incorporated. The input file is now more restrictive, but the requirements are fewer. The objective was to simplify the user's burden and facilitate the independent development of a graphical front end for user input and computed output. A graphical front end could be tailored to a specific software platforms, while the computational portion remains relatively platform independent.

8.1 Input File

In general, most of the parameters from 4SIGHT remain. In some cases, however, the expression has been compressed to facilitate the addition of parameter uncertainty. A number of parameters require a single value, others require the specification of a probability distribution (for parameter uncertainty Monte Carlo calculation), and still others allow for default values with a specified coefficient of variation. A useful means of describing the input file is to give an example:

```
21 N_cells
4 num_species
 8  0.000 0.300 0.000
19  0.000 0.200 0.000
11  0.200 0.100 0.000
17  0.200 0.000 0.000
0 1 free_surface_bool
0.02 0.0 pressure_MPa
-4 -9.00 0.500 permeability_cm/s
-3 1000. 0.25 formation_factor
-3 0.150 0.05 porosity
+3 0.500 0.05 wc
+3 20.0 1.00 fc_MPa
-3 20.0 0.10 Elastic_modulus_GPa
3  10.0 0.10 length_m
3  1.000 0.020 thickness_m
3  0.900 0.010 steel_depth_m
3  10.00 1.0 soil_depth_m
-3 0.010 0.050 As/Ac:reinforcement_ratio
100000. time_limit_days
23204 seed
10 simulations
```

The parameters shown will be discussed on a line by line basis. The optional text that follows each numerical parameter(s) is included as an aid to the user, but is ignored by the computer program.

Line 1: N_cells

The number of finite difference computational elements used to represent the slab for the 1-D calculation. A value of 21 is typically sufficient.

Line 2: num_species

The number of ionic species available for transport. The available ionic species are the following:

Key	Species
1	H ⁺
3	Li ⁺
11	Na ⁺
12	Mg ⁺²
19	K ⁺
20	Ca ⁺²
6	CO ₃ ⁻²
7	NO ₃ ⁻
8	OH ⁻
16	SO ₄ ⁻²
17	Cl ⁻
35	Br ⁻
53	I ⁻

In this example there are four species: OH⁻, Cl⁻, K⁺, Na⁺.

Line 2a,2b,.. :

The quantity of each of the num_species present. The four values given (AtNo cA cInt cB) are as follows:

AtNo : atomic number of species. In the case of OH⁻ and SO₄²⁻, it is the atomic number of the first species. Ex.: OH⁻ = 8, SO₄²⁻ = 16, etc.

cA : molarity of species external to *Side A*.

cInt : molarity of species within the concrete.

cB : molarity of species external to *Side B*.

Side A and Side B are arbitrary.

Line 3: free_surface_bool

A boolean value, either 0 or 1, denoting whether *Side A* or *Side B* is a **free_surface**. For a **free_surface**, the diffusive flux is zero and ions within the pore solution accumulate in the presence of a Darcy flow.

Line 4: pressure_MPa

The hydrostatic pressure at *side 0* and *side 1*, in units of MPa.

n.b.: For some of the following parameters, the user is to supply 4SIGHT with information regarding the type of distribution to use and the parameters of that distribution: x_o and σ . The meaning of the distribution parameters have been discussed previously. The particular distribution is specified using the following numbering scheme:

n = 1 : delta function

n = 2 : uniform distribution

n = 3 : Gaussian distribution

n = 4 : Lognormal distribution

If the user is specifying a definite value (and not relying upon 4SIGHT to create and estimated value for them), the distribution type n is made positive using a leading plus sign. If the distribution type n is made negative with a leading minus sign, 4SIGHT will generate a default value based on the remaining specified values. If a default value is requested, the value for x_o appearing in the input file will be ignored and the user specifies the *coefficient of variation* of this default value through the parameter σ . The exception to this is the hydraulic conductivity: if its distribution type n is negative, σ represents the standard deviation of the logarithm, which is identical to its meaning for positive values of the distribution type. The relationships used by 4SIGHT to calculate default values either appear in this report or can be found in the previous 4SIGHT report [1].

Line 5: permeability_cm/s

The logarithm (base 10) of the hydraulic conductivity of uncracked concrete, when expressed in units of cm/s. The three values shown are the distribution type, x_o , and σ . In the example, the user is requesting that the computer estimate the hydraulic conductivity, and that the standard deviation of the logarithms (base 10) of these values be 0.500. This corresponds to hydraulic conductivity values varying over one half and order of magnitude.

Line 6: formation_factor

The formation factor of the intact concrete. The three numbers are the distribution type, x_o , and σ . In the example above, the user is requesting 4SIGHT to estimate the formation factor from the other parameters, and that these predicted values will have a coefficient of variation of 25 %.

Line 7: porosity

The capillary porosity of the intact concrete. The three numbers are the distribution type, x_o , and σ . In the example above, the user is requesting 4SIGHT to estimate the porosity from the other parameters, and that these estimated values will have a coefficient of variation of 5 %.

Line 8: wc

The water cement ratio at the time of mixing. The three numbers are the distribution type, x_o , and σ . In the example above, the user is specifying that the water cement ratio shall be chosen from a Gaussian distribution with mean 0.50 and standard deviation 0.05.

Line 9: fc_MPa

The design compressive strength of the concrete. The three numbers are the distribution type, x_o , and σ . In the example above, the user is specifying that the compressive strength shall be chosen from a Gaussian distribution with mean 20 MPa. and standard deviation 1.0 MPa.

n.b.: At least one of the above six parameters must be specified by the user. Therefore, at least one of these values must have a positive distribution type. Otherwise, 4SIGHT has no information from which to characterize the concrete. Of course, the user may specify all of these parameters. In the above input file, the + and - are used to remind the user of this requirement.

Line 10: Elastic_modulus_GPa

The elastic modulus of the concrete, in units of GPa. The three numbers are the distribution type, x_o , and σ . In the example above, the user is specifying that the elastic modulus be estimated from the other material parameters, and that these values be chosen to have a coefficient of variation of 10 %.

Line 11: length_m

The length of the slab, in units of m. The three numbers are the distribution type, x_o , and σ . In the example above, the user is specifying that the length be estimated from a Gaussian distribution with mean 10.00 and standard deviation 0.10.

Line 12: thickness_m

The vertical thickness of the slab, in units of m. The three numbers are the distribution type, x_o , and σ . In the example above, the user is specifying that the thickness be estimated from a Gaussian distribution with mean 1.00 and standard deviation 0.02.

Line 12: steel_depth_m

The depth of reinforcement steel, in units of m. The three numbers are the distribution type, x_o , and σ . In the example above, the user is specifying that the depth of steel reinforcement be estimated from a Gaussian distribution with mean 0.90 and standard deviation 0.01.

Line 12: soil_depth_m

The depth of soil over the vault, in units of m. The three numbers are the distribution type, x_o , and σ . In the example above, the user is specifying that the depth of steel reinforcement be estimated from a Gaussian distribution with mean 10.00 and standard

deviation 1.00.

Assigning a negative value to the depth of soil informs 4SIGHT that the user does not want a crack analysis, and that the concrete should remain entirely intact, without any cracks.

Line 12: As/Ac:reinforcement_ratio

The reinforcement ratio, defined as the ratio of the area of steel (**As**) to the area of concrete (**Ac**). The three numbers are the distribution type, x_o , and σ . In the example above, the user is specifying that 4SIGHT should estimate a “best” guess from the available data and that deviates should have a coefficient of variation of 5 %.

Line 12: time_limit_days

The time limit for the service life calculation, in units of days.

Line 12: seed

A seed for the random number generator. Using the same seed will result in identical values being generated.

Line 12: simulations

The number of times to perform a parameter uncertainty calculation.

9 Summary

These efforts directed towards 4SIGHT have moved it towards a rigorous model of advective-diffusive transport within concrete. This is a fundamental part of establishing a service life model based on the simulation of reactions within the concrete. Every degradation mechanism relevant to concrete performance depends, in some way, on the transport characteristics of the material. Although applying transport models to both reference data and carefully controlled experiments appear to be logical endeavors, they are rare procedures in the concrete materials research literature.

The work done for this project has shown that a carefully constructed model that accounts for ion-ion interactions, due to both electrostatic interactions and excluded volume interactions, can then be used to model “real world” behavior. Further, the resulting transport equation reveals the meaningful physical quantities that are required from experiments performed on the material of interest. It was serendipitous that the more rigorous equation actually requires fewer physical parameters, regardless of the number of different species being transported.

An unforeseen result of this work has been a critical evaluation of the meaningfulness of the apparent diffusion coefficient. Experiments verified theoretical expectations that the apparent diffusion coefficient can vary over time in nonreacting porous systems. Data from experiments done here have shown that the apparent diffusion coefficient of a particular ion can vary by a factor of ten, depending on the other ionic species present. Further, a particular collection of species can lead to a *negative* apparent diffusion coefficient. In contrast, a rigorous transport equation, using a fixed porosity and formation factor, can capture this behavior by incorporating the ion-ion interactions into the transport equation.

The addition of a simple structural analysis into 4SIGHT will allow users to make, in the absence of a more thorough analysis, reasonable approximations of the width, depth, and spacing of drying shrinkage and flexural cracks. An analytical investigation of these relationships revealed that the most important factors influencing the bulk permeability of a reinforced concrete slab in flexure is the permeability of the uncracked concrete and the depth of the neutral axis. The permeability is insensitive to the details of the particular crack model employed.

The addition of a Monte Carlo calculation based on parameter uncertainty addresses the inherent issue of variability. A deterministic service life calculation is meaningless since it would be impossible to guarantee the predicted result. Rather, by at least incorporating the parameter uncertainty into the result, one can make a statement about the result uncertainty as a function of the parameter uncertainty. Further, a probabilistic result is a better representation of a physical problem since one can then ask for prediction intervals of the computed results.

References

- [1] K.A. Snyder and J.R. Clifton, “4SIGHT Manual: A computer program for modeling degradation of underground low level waste concrete vaults,” NISTIR 5612, National Institute of Standards and Technology, Gaithersburg, MD, 1995.
- [2] L.-O. Nilsson, P. Sandberg, E. Poulsen, Tang L., A. Andersen, and J.M. Frederiksen, “HETEK: A System for estimation of chloride ingress into concrete - Theoretical background,” Report No. 83, Road Directorate, Denmark Ministry of Transport, 1997.
- [3] *ACI Manual of Practice*, American Concrete Institute, 1998.
- [4] R.L. Blaine, H.T. Arni, B.E. Forster, R.A. Clevenger, L. Bean, and E.K. Hubbard, “Interrelations Between Cement & Concrete Properties, Part 1: Materials, Techniques, Water, Requirements and Trace Elements,” Building Science Series 2 (1965); J.R. Clifton and R.G. Mathey, “Interrelations Between Cement & Concrete Properties, Part 6: Compilation of Data from Laboratory Studies,” Building Science Series 36 (1971), National Bureau of Standards, U.S. Department of Commerce.
- [5] J. Trägårdh and B. Lagerblad, “Leaching of 90-year old concrete mortar in contact with stagnant water,” Technical Report, Swedish Cement and Concrete Research Institute, Stockholm, 1998.
- [6] P. Sandberg, L. Tang, and A. Andersen, “Recurrent studies of chloride ingress in uncracked marine concrete at various exposure times and elevations,” *Cement and Concrete Research* **28**, 1489–1503, 1998.
- [7] P. Sandberg and L. Tang, “A field study of the penetration of chlorides and other ions into a high quality concrete marine bridge column,” *Durability of Concrete* (SP-145), V.M. Malhotra, Ed., American Concrete Institute, 557–571, 1994.
- [8] L. Mejlbro, “The complete solution of Fick’s second law of diffusion with time-dependent diffusion coefficient and surface concentration,” *Durability of Concrete in Saline Environment* (Cementa AB, Sweden), 127–157, 1996.
- [9] J.M. Frederiksen and E. Poulsen, “HETEK: Chloride penetration into concrete - Manual,” Report No. 123, Road Directorate, Denmark Ministry of Transport, 1997.
- [10] I. Rubinstein, *Electro-Diffusion of Ions*, Society for Industrial and Applied Mathematics, Philadelphia, 1990.
- [11] M. Kato, “Numerical analysis of the Nernst-Planck-Poisson system,” *J. Theor. Bio.* **177**, 299–304, 1995.
- [12] A.E. James, J.D. Stillman, and D.J.A. Williams, “Finite element solution of the equations governing the flow of electrolyte in charged microporous membranes,” *Int. J. Numer. Meth. Fluids* **20**, 1163–1178, 1995

- [13] E. Samson and J. Marchand, “Numerical solution of the extended Nernst-Planck model,” *J. Coll. Interface Sci.* **215**, 1–8, 1999.
- [14] E. Samson and J. Marchand, “Modelling ion diffusion mechanisms in porous media,” *Int. J. Numer. Meth. Engin.* **46**, 2043–2060, 1999.
- [15] O. Truc, J.-P. Ollivier, and L. O. Nilsson, “Numerical solution of multi-species diffusion,” *Mater. Struct.* **33**, 566–573, 2000.
- [16] O. Truc, J.-P. Ollivier, and L.-O. Nilsson, “Numerical simulation of multi-species transport through saturated concrete during a migration test,” *Cem. Concr. Res.* **30**, 1581–1592, 2000.
- [17] K.S. Pitzer, “Thermodynamics of electrolytes. I. Theoretical basis and general equations,” *Journal of Physical Chemistry* **77**, 268–277, 1973. K.S. Pitzer and G. Mayorga, “Thermodynamics of electrolytes. II. Activity and osmotic coefficients for strong electrolytes with one or both ions univalent,” *Journal of Physical Chemistry* **77**, 2300–2308, 1973.
- [18] E.L. Cussler, *Multicomponent Diffusion*, Elsevier Scientific, 1976.
- [19] See any of the conference proceedings such as L.-O. Nilsson and J.P. Ollivier (eds.), *Chloride Penetration into Concrete*, RILEM, 1997. *Flow of Fluids Through Porous Materials*, Reinhold Publishing, 1961.
- [20] R.E. Collins, *Flow of Fluids Through Porous Materials*, Reinhold Publishing, 1961.
- [21] Bockris, J.O’M. and Reddy, A.K.N., *Modern Electrochemistry*, Volume 1, Plenum Press, 1970.
- [22] K.A. Snyder, C. Ferraris, N.S. Martys, and E.J. Garboczi, “Using impedance spectroscopy to assess the viability of the rapid chloride test for determining concrete conductivity,” *J. Res. NIST* **105**, 497–509, 2000.
- [23] R. Mills and V.M.M. Lobo, *Self-Diffusion in Electrolyte Solutions*, Elsevier, New York, 1989.
- [24] J. Crank, *The Mathematics of Diffusion*, Oxford University Press, 1975.
- [25] S. Torquato, “Random heterogeneous media: Microstructure and improved bounds on effective properties,” *Appl. Mech. Rev.* **44**, 37–76, 1991.
- [26] A.E. Scheidegger, *J. App. Phys.* **25**, 994, 1954.
- [27] J. Bear and Y. Bachmat, “A generalized theory on hydrodynamic dispersion in porous media,” in *Artificial Recharge and Management of Aquifers*, International Association of Scientific Hydrology, Publication 72, 7–16, 1967.
- [28] G. Matheron and G. de Marsily, “Is transport in porous-media always diffusive – A counterexample,” *Water Resour. Res.* **16**, 901, 1980.

- [29] D. Russo, *Water Resour. Res.* **20**, 1260, 1984.
- [30] *CRC Handbook of Chemistry and Physics* (63rd Edition), R.C. Weast (Ed.), CRC Press, Boca Raton, FL, 1982.
- [31] L.N. Plummer, D.L. Parkhurst, G.W. Fleming, and S.A. Dunkle, "A Computer Program Incorporating Pitzer's Equations For Calculation Of Geochemical Reactions In Brines," Water-Resources Investigations Report 88-4153, U.S. Geological Survey, Reston, VA, 310 pp., 1988.
- [32] K.A. Snyder, "Relationship Between Formation Factor and Diffusion Coefficient: Theory and Experiment," (Presented) Advances in Cement and Concrete (United Engineering Foundation), Quebec, Canada, August 2000.
- [33] K.A. Snyder and J. Marchand, "Effect of Speciation on Diffusive Transport in Non-Reactive Systems," (Presented) Symposium FF: Materials Science of High-Performance Concrete (Materials Research Society), Boston, MA, November 2000.
- [34] K.A. Snyder, "The relationship between the formation factor and the diffusion coefficient of porous materials saturated with concentrated electrolytes: Theoretical and experimental considerations," (Submitted to) *Concrete Science and Engineering*, 2000.
- [35] K.A. Snyder and J. Marchand, "Effect of speciation on the apparent diffusion coefficient in nonreactive porous systems," (Submitted to) *Cement and Concrete Research*, 2000.
- [36] R.E. McDuff and R.A. Ellis, "Determining diffusion-coefficients in marine-sediments – Laboratory study of the validity of resistivity techniques," *Am. J. Sci.* 279 (1979) 666–675.
- [37] F.A. Settle, ed., *Handbook of Instrumental Techniques for Analytical Chemistry*, Prentice Hall, 1997.
- [38] L.M. Schwartz, P.N. Sen, and D.L. Johnson, "Influence of rough surfaces on electrolytic conduction in porous media," *Phys. Rev. B* 40 (1989) 2450–2458.
- [39] H.J.V. Tyrrell and K.R. Harris, *Diffusion in Liquids*, Butterworths, 1984.
- [40] B.N. Taylor and C.E. Kuyatt, "Guidelines for Evaluating and Expressing the Uncertainty of NIST Measurement Results," National Institute of Standards and Technology, NIST Technical Note 1297, Gaithersburg, MD, 1993.
- [41] W.H. Press, B.P. Flannery, S.A. Teukolsky, and W.T. Vetterling, *Numerical Recipes*, Cambridge University Press, New York, 1988.
- [42] D.E. Knuth, *Seminumerical Algorithms*, 2nd ed., Vol. 2 of *The Art of Computer Programming*, Addison-Wesley, 1981.

- [43] M.J. Lighthill, *Introduction To Fourier Analysis and Generalised Functions*, Cambridge University Press, Cambridge, England, 1958.
- [44] G. Arfken, *Mathematical Methods for Physicists*, Academic Press, New York, 1970.
- [45] W.F. Espenscheid, M. Kerker and E. Matijević, “Logarithmic distribution functions for colloidal particles,” *Journal of Physical Chemistry* **68**, 3093–3097, 1964.
- [46] P.J. Uno, “Plastic shrinkage cracking and evaporation formulas,” *ACI Materials Journal* **95**, 365–375, 1998.
- [47] K.A. Snyder, “Effect of Drying Shrinkage Cracks and Flexural Cracks on Concrete Bulk Permeability,” NISTIR 6519, National Institute of Standards and Technology, Gaithersburg, MD, 2000.
- [48] A.H. Nilson and G. Winter, *Design of Concrete Structures* (Tenth Edition), McGraw-Hill, 1986.
- [49] G.D. Base and M.H. Murray, “A new look at shrinkage cracking,” *Civil Engineering Transactions* (Australia) **CE 18**, No. 2, 171–176, 1982.